JGR Solid Earth

RESEARCH ARTICLE
10.1029/2025JB031716

Rift-Related Sedimentary Basin and Deeper-Seated Mafic Intrusions Modeled Beneath Thwaites Glacier, West Antarctica: Influence on Glacier Dynamics

Louise Borthwick[1], Atsuhiro Muto[1], Sridhar Anandakrishnan[2], Kirsty Tinto[3], Ronan Agnew[4], Alex Brisbourne[4], Rebecca Schlegel[5], Siobhan Killingbeck[6], Bernd Kulessa[6], Richard Alley[2], Amanda Willet[2], and Sierra Melton[2]

[1]Department of Earth and Environmental Science, Temple University, Philadelphia, PA, USA, [2]Department of Geosciences, The Pennsylvania State University, University Park, PA, USA, [3]Lamont-Doherty Earth Observatory, Columbia University, Palisades, NY, USA, [4]British Antarctic Survey, Cambridge, UK, [5]Department of Geosciences, University of Tübingen, Tübingen, Germany, [6]School of Biosciences, Geography and Physics, Swansea University, Swansea, UK

Abstract Thwaites Glacier in West Antarctica has been identified as a route to destabilization of the whole West Antarctic Ice Sheet, potentially leading to several meters of sea-level rise. However, future evolution of Thwaites Glacier remains uncertain due to a lack of detailed knowledge about its basal boundary that will affect how its retreat proceeds. Here we aim to improve understanding of the basal boundary in the lower part of Thwaites Glacier by modeling the crustal structures that are related to the bed-type distribution and therefore influence the basal slip. We combine long-offset seismic, and gravity- and magnetic-anomaly data to model the crustal structures along two ~120 km lines roughly parallel to ice flow. We find a sedimentary basin ~40 km in length in the along-flow direction, with a maximum thickness of 1.7 ± 0.2 km, and two mafic intrusions at 5–10 km depth that vary in maximum thickness between 3.8 and 8.6 km. The sedimentary basin and major mafic intrusions we modeled are likely related to the multi-stage tectonic evolution of the West Antarctic Rift System. Thwaites Glacier flows across a tectonic boundary within our study site, indicating it flows across tectonically formed structures. The varying geology and resulting variations in bed types demonstrate the influence of tectonics on Thwaites Glacier dynamics.

Plain Language Summary Thwaites Glacier, located in West Antarctica, contains enough ice to raise the global sea level by more than two feet and its retreat could initiate the collapse of the whole West Antarctic Ice Sheet. However, the timing and the magnitude of the retreat of Thwaites Glacier remains unclear. This is in part because of limited knowledge of the geology beneath the glacier such as the type of material under the ice, availability of geothermal heat and availability of water, all of which dictate the slipperiness at the glacier bed. Here we investigate the geologic structures underneath lower parts of Thwaites Glacier using a combination of long-offset seismic, gravity and magnetic methods. We find a sedimentary basin with maximum thickness of around 1.5 km beneath the glacier and two intrusions of dense, mafic rock around the middle of the crust. These geologic structures likely originate from rifting processes that occurred in this region 25–90 million years ago. Thwaites Glacier is flowing across these rift-related geologic structures and how it retreats in the future will be influenced by variability in the basal slipperiness resulting from these geologic structures.

Key Points:

- Seismic, gravity and magnetic data used to model a sedimentary basin and deep-seated mafic intrusions beneath lower parts of Thwaites Glacier
- Thwaites Glacier flows over a rift-related boundary that results in variable bed types
- Crustal structures identified were likely formed during one of the phases of crustal extension that formed the West Antarctic Rift System

Correspondence to:
L. Borthwick and A. Muto,
louise.borthwick@temple.edu;
amuto@temple.edu

Citation:
Borthwick, L., Muto, A., Anandakrishnan, S., Tinto, K., Agnew, R., Brisbourne, A., et al. (2025). Rift-related sedimentary basin and deeper-seated mafic intrusions modeled beneath Thwaites Glacier, West Antarctica: Influence on glacier dynamics. *Journal of Geophysical Research: Solid Earth*, *130*, e2025JB031716. https://doi.org/10.1029/2025JB031716

Received 18 APR 2025
Accepted 12 SEP 2025

Author Contributions:
Conceptualization: Atsuhiro Muto, Sridhar Anandakrishnan
Data curation: Louise Borthwick
Formal analysis: Louise Borthwick
Funding acquisition: Atsuhiro Muto, Sridhar Anandakrishnan, Alex Brisbourne, Bernd Kulessa, Richard Alley
Investigation: Louise Borthwick, Sridhar Anandakrishnan, Ronan Agnew, Alex Brisbourne, Rebecca Schlegel, Siobhan Killingbeck, Amanda Willet, Sierra Melton
Methodology: Louise Borthwick, Atsuhiro Muto, Kirsty Tinto, Ronan Agnew, Alex Brisbourne, Siobhan Killingbeck, Bernd Kulessa, Richard Alley
Project administration: Sridhar Anandakrishnan, Alex Brisbourne

1. Introduction

The West Antarctic Ice Sheet (WAIS), which contains enough ice to raise global sea level by more than 5 m (Morlighem et al., 2020; Naughten et al., 2023), is currently losing mass at an increasing rate (The IMBIE Team, 2018). The main driver behind this increasing ice-mass loss is the glaciers within the Amundsen Sea Embayment (ASE) which showed an increase in ice discharge of 77% between 1973 and 2013 (Mouginot et al., 2014). Of the glaciers in the ASE, Thwaites Glacier (Figure 1) has been identified as the most-likely route to the collapse of the WAIS (Scambos et al., 2017) due to its large drainage basin and its inland deepening bed, causing it to be susceptible to marine ice sheet instability (MISI) (Schoof, 2012; Weertman, 1974). Additionally, once Thwaites Glacier loses its buttressing ice shelf and starts retreating into the deep basin, tall ice cliffs susceptible to collapse may be exposed, leading to unprecedented rapid ice loss and sea-level rise through marine ice cliff instability (DeConto et al., 2021; Pollard et al., 2015). Although the importance of Thwaites Glacier to the

Resources: Atsuhiro Muto, Sridhar Anandakrishnan, Alex Brisbourne
Software: Louise Borthwick
Supervision: Atsuhiro Muto, Sridhar Anandakrishnan, Kirsty Tinto
Visualization: Louise Borthwick
Writing – original draft: Louise Borthwick
Writing – review & editing: Louise Borthwick, Atsuhiro Muto, Kirsty Tinto, Ronan Agnew, Alex Brisbourne, Rebecca Schlegel, Siobhan Killingbeck, Bernd Kulessa, Richard Alley, Amanda Willet, Sierra Melton

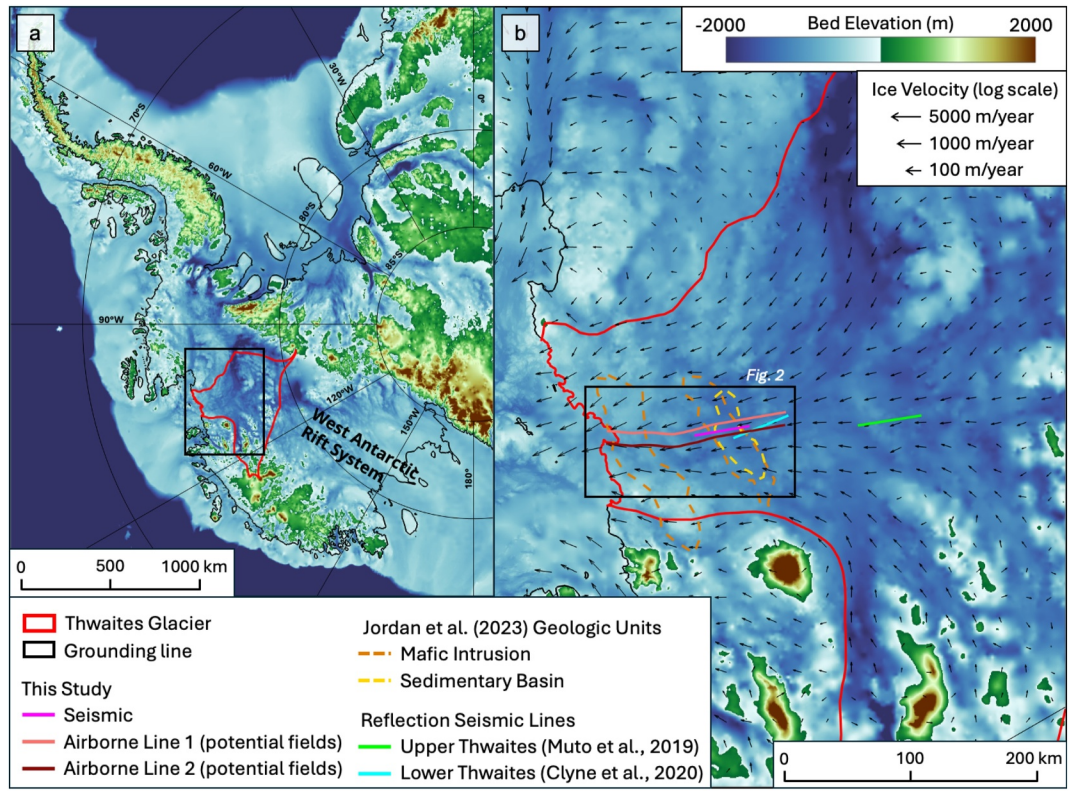

Figure 1. (a) West Antarctica with location of (b) shown in black box. (b) Thwaites Glacier with selected geologic units from Jordan et al. (2023), previous seismic reflection surveys and current study seismic and potential fields lines. Background is MEaSUREs BedMachine Antarctica V3 bed elevation (Morlighem, 2022). All elevations are referenced to the WGS84 ellipsoid. Vectors show the ice-flow velocity from MEaSUREs InSAR Phase-Based Antarctica Ice Velocity Map (Mouginot et al., 2019). Black box shows the location of Figure 2. This figure was created using the Antarctic Mapping Tools (Greene et al., 2017).

stability of the WAIS is well recognized, the timing and the magnitude of its retreat remains unclear because of poorly constrained boundary conditions, particularly at the ice-sheet base, allowing widely varying predicted outcomes (e.g., Larour et al., 2019; Parizek et al., 2013; Schwans et al., 2023).

The ice-sheet basal boundary exerts a fundamental control on ice-sheet dynamics through topographic steering of ice flow (e.g., Anandakrishnan et al., 1998; Bell et al., 1998; Bingham et al., 2012), distribution of basal sediments (e.g., Bell et al., 1998; Peters et al., 2006; Smith et al., 2013) and bed type (Koellner et al., 2019; Muto et al., 2019; Schwans et al., 2023), flow of geothermal heat (e.g., Dziadek et al., 2021; Joughin et al., 2009; Schroeder et al., 2014) and flux of subglacial water (e.g., Christoffersen et al., 2014; Fricker et al., 2007; Siegert et al., 2018). The distribution of bed types is particularly important to the evolution and sea-level contribution of Thwaites Glacier and the WAIS. Bed-type distribution refers to whether the bed is rigid and made of non-deforming rock or non-deforming sediments ("hard" bed) or made of saturated, deforming sediments ("soft" bed) (e.g., Alley et al., 2022). These bed types can be parameterized in ice-sheet models using a power-law rule for basal slip with a different power exponent, and have been shown to cause varying retreat patterns. On Thwaites Glacier, modeling has shown that the glacier retreat will proceed differently if the bed is composed entirely of soft bed or hard bed (Parizek et al., 2013), or if it is a combination of both (Koellner et al., 2019; Schwans et al., 2023).

Despite its importance, the bed-type distribution beneath Thwaites Glacier has only been mapped in detail at two locations; Upper Thwaites (Muto et al., 2019) (green line in Figure 1b) and Lower Thwaites (Clyne et al., 2020) (cyan line in Figure 1b). These studies used reflection-seismic data to determine the bed type based on the acoustic impedance, each over a ~40-km survey line along ice flow. They found continuous soft bed in relatively flat, low-lying areas, and a mix of hard and soft bed over relatively high and more undulating areas. Such variations in continuous soft and mixed beds are in contrast to typical fast-flowing glaciers and ice streams that flow over

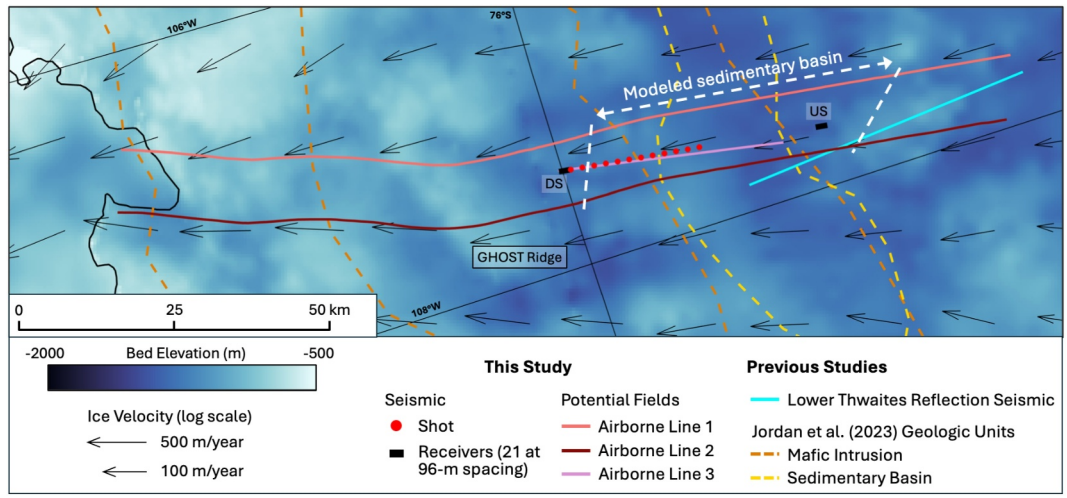

Figure 2. Study site map. Background is bed elevation from MEaSUREs BedMachine Antarctica V3 (Morlighem, 2022) and from swath radar over Lower Thwaites grid (Holschuh et al., 2020). Receiver arrays are labeled upstream (US) and downstream (DS). Vectors show the ice-flow velocity from MEaSUREs InSAR Phase-Based Antarctica Ice Velocity Map (Mouginot et al., 2019). Dashed white lines indicate the extent of the sedimentary basin modeled in this study. This figure was created using the Antarctic Mapping Tools (Greene et al., 2017).

continuous soft bed, allowing rapid flow by deforming till (e.g., Bingham et al., 2012; Blankenship et al., 1986; Peters et al., 2006; Shepherd et al., 2006; Smith et al., 2013). The observations of varying bed types beneath Thwaites Glacier indicate that to accurately project future sea-level changes, models need to account for variable bed types rather than using a single flow law across the whole catchment, as the majority of large-scale modeling studies do (e.g., DeConto et al., 2021; Morlighem et al., 2024). However, currently there are no data beyond the two reflection-seismic lines to precisely map the bed type distribution.

The bed-type distribution has been linked to crustal structures resulting from tectonics in a number of locations within West Antarctica. The majority of the WAIS sits on extended, subsided crust of the West Antarctic Rift System (WARS), with a well defined southern boundary at the Transantarctic Mountains, and a less well defined northern boundary around Marie Byrd Land and into the Amundsen Sea (Ferraccioli et al., 2002; Jordan et al., 2020). The history of the WARS development is summarized by Jordan et al. (2020); Jordan et al. (2023); Siddoway (2008). A number of fast-flowing glaciers and ice streams in West Antarctica, including Thwaites Glacier, lie within the currently known WARS, some of which flow along rift-formed geologic structures. Siple Coast Ice Streams (Anandakrishnan et al., 1998; Bell et al., 1998; Peters et al., 2006; Rooney et al., 1991), Ferrigno Ice Stream (Bingham et al., 2012) and Pine Island Glacier (Smith et al., 2013) all flow within rift-formed, fault-bounded sedimentary basins, characterized by smooth, flat beds capped by soft, deforming sediments. Thwaites Glacier instead flows across a series of ridges and troughs (Figure 1), indicating it may flow across rift-formed crustal structures rather than being confined by them.

Basin-wide crustal structures under Thwaites Glacier have been mapped using airborne potential field and radar data by Jordan et al. (2023) (selected structures in Figure 1). The sedimentary basins and mafic intrusions in this map are orientated roughly perpendicular to ice flow, demonstrating Thwaites Glacier flows across the tectonic fabric. They additionally outline sedimentary basins that coincide with the continuous soft bed at Upper and Lower Thwaites. They outline sedimentary basins where the ice-basal roughness is low, which provides an estimate of their extent but gives no measurement of basin thickness. Additionally, in some locations, contrasting signals (e.g., high-relief topography mapped by radar and low Bouguer gravity anomaly typical of thick sediments) cause multiple geologic structures to be outlined at the same location. Due to the non-unique nature of potential-fields methods, the thickness and position of these structures can only be delineated within the crust indirectly by modeling. Additional constraints from methods such as long-offset seismic reflection/refraction (Peters et al., 2006) are needed to map the geometry of these crustal structures.

In this study, we model the crustal structures with a focus on the upper crust at a study site close to the Lower Thwaites reflection seismic line (Figure 2). At this location, there is a contrasting signal of smooth bed, indicative

of a sedimentary basin, and gravity and magnetic anomaly highs, indicating a mafic intrusion. We unravel the contrasting signals with multiple geophysical data sets. We use long-offset reflection/refraction seismic data to determine the thickness of the sedimentary basin and the density of the sediments. We then use airborne gravity- and magnetic-anomaly data to model the mafic intrusions, given the seismic constraint on the sedimentary basin. We perform modeling in 2D along seismic and potential-field survey lines to estimate the depth and the thickness of bodies and compare their length to those in the geologic map of Jordan et al. (2023). Determining the geometry of these bodies will give additional insight into the link between bed type and rifting on Thwaites Glacier. Our method requires the results from the seismic data to constrain the crustal-structure modeling with potential-fields data. Therefore, we first present the seismic method and its results, and then the potential-field methods and their results, in separate sections. We then discuss the potential formation mechanisms of the modeled crustal structures and how they relate to Thwaites Glacier dynamics.

2. Study Area

This study is part of the International Thwaites Glacier Collaboration (ITGC) Geophysical Habitat of Subglacial Thwaites (GHOST) project. Our study area covers the lower ∼125 km of the main trunk of Thwaites Glacier, straddling a topographic high named GHOST Ridge, which has been identified as a potential future stabilizing point (e.g., Schwans et al., 2023). Our data consists of a long-offset seismic reflection/refraction survey and airborne gravity- and magnetic-anomaly data collected as part of the ITGC (Jordan & Robinson, 2021a, 2021b) (Figure 2). The seismic-survey line is 44-km long and located ∼17 km upstream of GHOST Ridge. The downstream half of this survey line covers undulating bed topography and the upstream half is over an area of smooth, low-lying bed topography. Over this smooth, low-lying area, Clyne et al. (2020) found continuous soft bed and Jordan et al. (2023) outlined a sedimentary basin. There are no airborne potential-field lines exactly coincident with our seismic line, so we use two lines ∼5 km to the east and west of our seismic line, each ∼125-km long. These potential-field lines include both gravity- and magnetic-anomaly data and show highs in both of the anomalies where Jordan et al. (2023) have outlined mafic intrusions.

3. Seismic Methods and Results

3.1. Data Collection

The seismic data were collected in the 2023/24 Antarctic field season as part of the ITGC GHOST field work. The seismic line was ∼44-km long with receiver arrays at each end, and shots between the arrays with a minimum offset of 0 km and maximum offset of ∼42 km. Receivers used were Magseis Fairfield Z-Land, Generation 2, 5 Hz three-component nodes (Ringler et al., 2018) programmed to record at 1,000 Hz with a pre-amp gain of 36 dB, linear phase Nyquist filter and DC offset removal. Each array was composed of 21 nodes at 96-m intervals, covering a total distance of 1.92 km, and the arrays were separated by 40.32 km (Figure 2). In the upstream array, there were 2 nodes placed at each location but at the downstream array, only 8 downstream-most locations had 2 nodes placed due to limited node availability, giving a total of 71 nodes deployed. Nodes were buried at ∼5-cm deep to their top, leveled with a bubble level and the N-S component was aligned with the azimuth of the survey line. Locations of the nodes were determined using real-time kinematic surveying with Stonex S900+ GNSS receivers. For post-processing, we additionally recorded the positions of the nodes at each end of the arrays with a Stonex receiver and processed them using the Canadian Spatial Reference System Precise Point Positioning service. These processed end-node positions were then used to determine the corrected positions for each node location in the arrays.

Shots were at 1.92 km intervals along the line, with the first shot (shot number 1 in Table 1) at the upstream-most receiver of the downstream array (Figure 2). Due to time and weather constraints, only 12 shots could be completed. The locations of the shots were determined in the field using real-time kinematic surveying, then later corrected with the post-processed position of the associated base station, in the same manner as the node positions explained above. Shots varied in size (see Table 1) and were composed of combined 1-kg Pentolite boosters. Shot depths also varied, Table 1, with the majority of shots between 30- and 40-m deep. All shots except numbers 10–12 were backfilled with snow after the explosives were inserted and left to sinter for at least 1 day. Due to time constraints, shots 10–12 were loaded and detonated immediately without backfilling. The shots were all carried out in one day with calm conditions in the morning and increasing wind in the afternoon, which affected shots 7–12.

Table 1
Shot Information

Shot number	Depth (m)	Size (kg)	Notes
1	33	14	
2	34	14	
3	38	14	
4	39	14	
5	21	14	
6	36	14	
7	17	14	
8	15	14	
9	15.5	14	
10	36.5	16	Not backfilled
11	35.5	17	Not backfilled
12	35	27	Not backfilled

Note. Shot number 1 refers to most downstream shot.

3.2. Identifying Arrivals

To identify arrivals that appear across multiple shots, we first combine and sort all the individual shot gathers by offset to produce a supergather for each receiver array. The traces were first stacked where two nodes were placed at the same location. For the supergathers, a bandpass filter of 18–26 Hz and automatic gain control with window of 600 ms were applied. The filtered and AGC-applied supergathers of the vertical component for the upstream and downstream receiver arrays are shown in Figures 3 and 4, respectively.

Before identifying arrivals from layers beneath the ice, we first model the travel times of reflections and refractions from the ice-bed interface. This is to ensure we do not misinterpret the sub-ice-bottom arrivals that we are targeting with the arrivals from the ice-bed interface. For this and all travel-time modeling, we use the forward ray-tracing part of the RAYINVR program (Zelt & Smith, 1992). We use the bed elevation from MEaSUREs BedMachine Antarctica V3 (Morlighem, 2022) (hereafter referred to as BedMachine) and the ice-surface elevation from the Reference Elevation Model of Antarctica (REMA) (Howat et al., 2022). We include a firn layer in the upper 164 m of the glacier with the thickness and velocity of sublayers determined from shallow refraction-seismic data collected at Upper Thwaites (Horgan et al., 2011).We do not have a measurement of the *P*-wave velocity of ice, so we use 3.85 km/s (Clyne et al., 2020) for this initial modeling, but this is varied later in the inversion.

We identify refracted arrivals on the vertical component in both the upstream and downstream supergathers (Figures 3 and 4). These refracted arrivals have a travel time greater than that modeled for a refracted arrival from the ice-bed interface (example shown with bed V_p of 5.8 km/s in Figures 3 and 4). This delay indicates that the refracted arrival is instead traveling along the base of a layer beneath the ice with V_p less than that of the ice. We additionally identify reflections from the base of this low-velocity layer. On the vertical component of the upstream array, we see a reflection at approximately 5.9 s at 20 km offset (US1 on Figure 3), which we interpret as the *P*-wave reflection from the base of the low-velocity layer as it arrives after the ice-bed *P*-wave reflection and before the ice-bed *S-p* converted-phase reflection. On the downstream array, there are arrivals that are too close together in time to distinguish on the filtered supergather. On the raw data from shot 5 (Figure 5) we see two

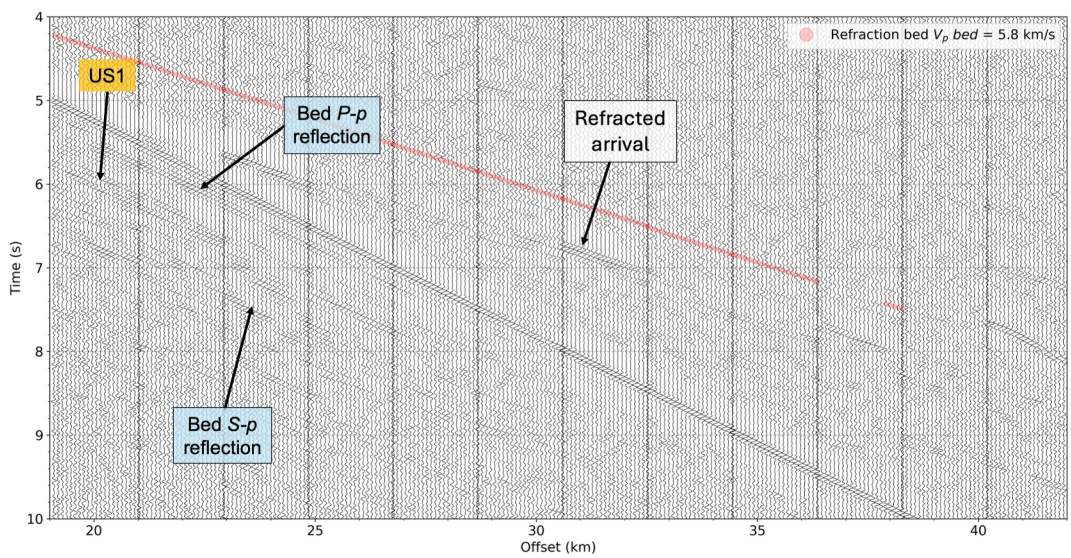

Figure 3. Supergather of the vertical component of the upstream array. Processed with a 18–26 Hz bandpass filter and automatic gain control with a window of 600 ms. Modeled ice-bed reflections are labeled with blue background. Modeled refraction from ice-bed interface shown in red for bed with V_p = 5.8 km/s. US1 = upstream reflection 1.

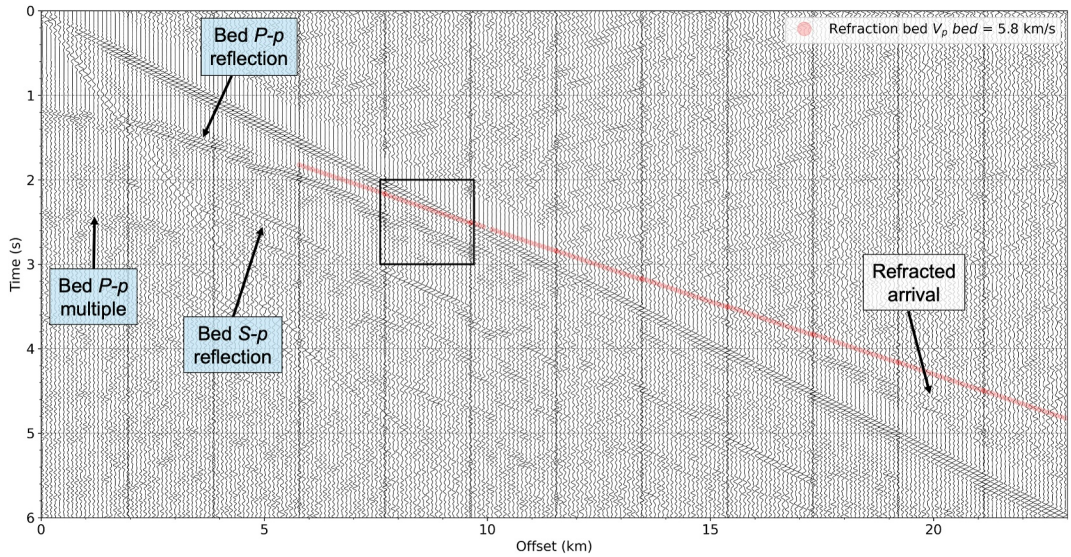

Figure 4. Supergather of the vertical component of the downstream array. Processed with a 18–26 Hz bandpass filter and automatic gain control with a window of 600 ms. Modeled ice-bed reflections in labeled with blue background. Modeled refraction from ice-bed interface shown in red for bed with V_p = 5.8 km/s. Black box shows times and offsets shown in Figure 5.

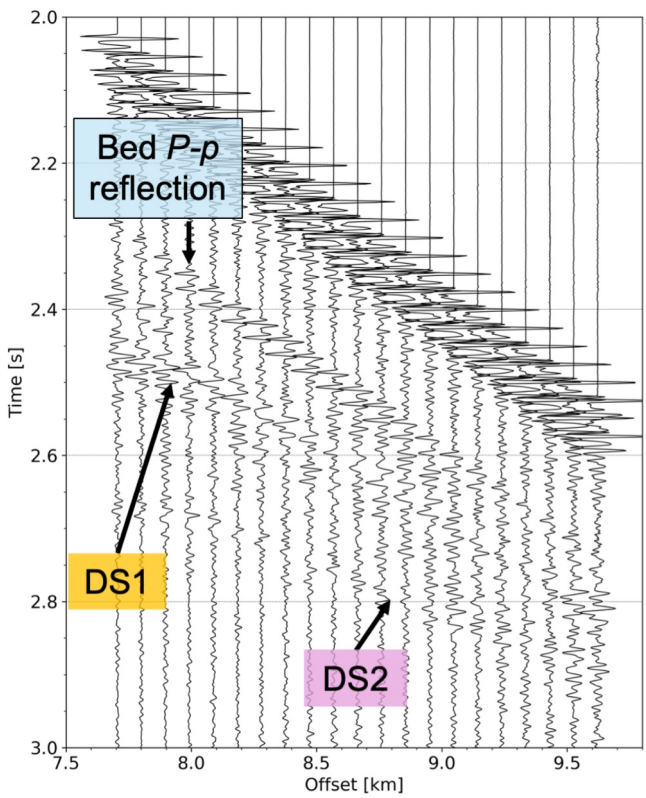

Figure 5. Arrivals on the downstream node array vertical component from shot number 5. DS1 = downstream reflection 1. DS2 = downstream reflection 2.

reflections, labeled DS1 and DS2. As DS1 is the first arrival after the ice-bed *P*-wave reflection, we interpret it as the *P*-wave reflection from the base of the low-velocity layer. DS2 could not be consistently identified across multiple shots, we do not include it in our interpretation.

3.3. Picking

We pick the arrivals from the low-velocity layer on individual shot gathers, rather than the supergather, to obtain travel time-offset pairs. The arrivals were not clear enough to be consistently picked without filtering applied to the data. Picking on data with a bandpass filter applied introduces a time shift and additional uncertainty to the data from this time shift (Table 2). However, we determined that the ability to confidently pick the same arrival across multiple shots outweighs the additional uncertainty introduced from filtering (see Section 3.4). Due to the varying frequency content and amplitudes across different arrivals, we used bandpass filters with a number of different frequencies (Table 2). To correct for the time shift associated with the filtering, we additionally pick the ice-bed *P*-wave reflected arrival (which is clear without filtering) both without filtering and with each of the filters used on other arrivals. We then calculate the difference in picked arrival times between those on the filtered and unfiltered data, and take the mean of the differences as the time shift for each applied filter (Table 2). Each of the arrivals were picked twice and only the picks consistent across both attempts were kept. We picked all the arrivals on the vertical component as they appeared the strongest on this component.

3.4. Uncertainty

The uncertainty in the travel-time data was determined by combining uncertainty in the firn travel time, bed elevation, shot depth and picking. We use a value of 1 ms for travel-time uncertainty in the firn (Peters et al., 2006). Bed-elevation uncertainty is the mean of the reported uncertainty of BedMachine

Table 2
Processing Applied During Picking of Each of the Arrivals

Arrival	Array	Component used	Filter frequencies (Hz)	Filter time shift (ms)	Filter time uncertainty (ms)
Headwave	Upstream	Vertical	5, 15, 18, 26	−39.77	6.98
Headwave	Downstream	Vertical	5, 15, 18, 26	−39.77	6.98
Reflection 1	Upstream	Vertical	5, 15, 30, 40	−21.66	5.06
Reflection 1	Downstream	Vertical	5, 15, 30, 40	−21.66	5.06

Note. Filter frequency refers to the corner frequencies of the bandpass (Ormsby) filter.

elevation along our survey line. We estimate the shot-depth uncertainty to be 5 m based on variation in depth measurements made in the field. To determine the uncertainty on the travel time due to the bed elevation and shot depth, we model the ice-bed *P*-wave arrival 100 times, applying Gaussian perturbations to bed elevation and shot depths consistent with their respective uncertainties. We then take the standard deviation of the *P*-wave arrival times for the 100 perturbed runs, which results in an uncertainty of 1 ms for the bed elevation and the shot depth. We define the picking uncertainty as the absolute difference in travel times between the two picking attempts on the data. This is calculated for each shot-receiver pair separately, as some arrivals are clearer than others, and has a mean value of 6 ms and standard deviation of 15 ms across the data. An additional uncertainty on the picking is introduced due to filtering. We define the filtering uncertainty as the standard deviation of the differences between the picked raw and filtered data from the ice-bed *P*-wave reflection (Table 2). All of these contributions are combined using root-sum squared to give an overall uncertainty for each shot-receiver pair, with a mean of 11 ms and a maximum of 104 ms.

3.5. Inversion

To derive a model that fits the seismic data within the uncertainty, we perform a travel-time inversion using a very fast simulated annealing algorithm. Very fast simulated annealing has been applied to seismic travel-time inversion by Roy et al. (2005) and we refer readers to this paper for the details of the method, including its merits over other inversion schemes. For our inversion, we again use the forward ray-tracing part of RAYINVR to forward model travel times. We compare forward-modeled travel times at each iteration of the inversion to the observed travel times by computing the root-mean-squared (RMS) misfit. The observed travel times are the picked refracted and reflected arrivals from the base of the low-velocity layer that we described in Section 3.2. The parameters we vary are the low-velocity layer thickness and velocity, and the basement-rock velocity. The inversion aims to reduce the misfit to below the tolerance. The tolerance is defined as the mean of the RMS misfits between the measurements and the measurements with Gaussian perturbations consistent with their uncertainty. Our inversion does not reach the tolerance, likely due to the lack of shots on the upstream half of the survey line, reducing the amount of data available to sufficiently constrain the model. Therefore, we instead end each inversion run when no improved solution has been found for 1,000 consecutive iterations. We repeat this process 100 times to obtain a distribution of results and take the mean of the distribution for each parameter to be the final model value and the 95% confidence interval as the parameter uncertainty.

The model is composed of 4 layers; firn, ice, low-velocity layer and basement rock. The firn and ice layers are described in Section 3.2. As the V_p in ice is not known precisely, we allow it to vary during the inversion within a range of 3.78–3.88 km/s, determined based on previous studies on Thwaites Glacier (Clyne et al., 2020; Muto et al., 2019) and Pine Island Glacier (Smith et al., 2013). For each inversion run a value within this range is randomly chosen. The firn layer is composed of 35 sublayers, each of which is input as a single thickness across the whole model. The ice-layer thickness is input to the model by discretizing into points at 500-m spacing, based on the resolution of the bed elevation data (Morlighem, 2022). The low-velocity-layer thickness is discretized into 20 points, giving spacing of ∼2.4 km. This spacing was found to optimize inversion efficiency while capturing sufficient variations in layer thickness. The basement rock is treated as a half-space, so we only need to define its velocity. All the layers have a single velocity applied to them. We also note that the edges of the model are 500 m beyond the extent of the data due to the modeling-program requirement.

We have minimal information on the V_p of the low-velocity layer and the basement rock. The arrival time of the refraction indicates the low-velocity layer has V_p less than that of the ice and therefore we set the limits to 2 and

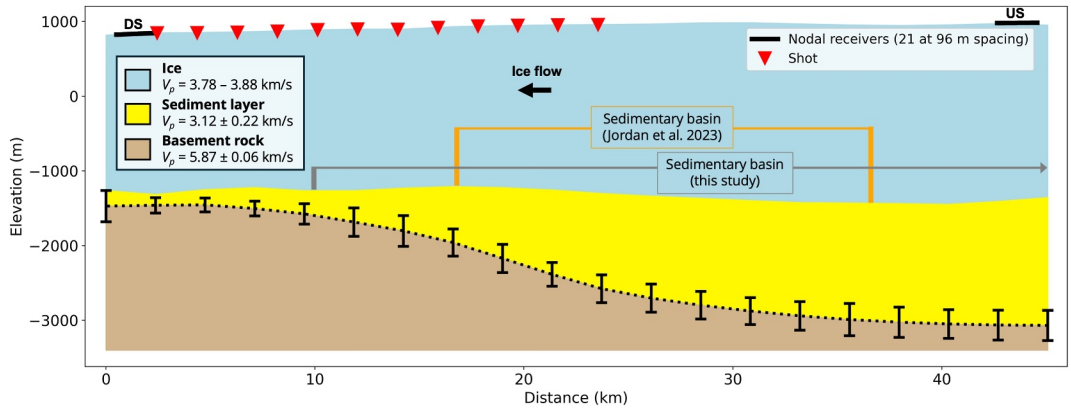

Figure 6. Results of the seismic travel-time inversion. Legend shows velocity of each layer with associated uncertainty from the inversion. Base of sediment layer is interpolated between mean values at each of the 20 inversion points. Each inversion point also shows the 95% confidence interval. The extent of the sedimentary basin is shown as we define (gray lines) and as defined by Jordan et al. (2023) (orange lines). Note that we do not define the upstream edge as we do not observe it. DS = downstream receiver array. US = upstream receiver array.

3.5 km/s. Based on the slope of the refracted arrival, we first estimate the basement-rock V_p to be about 5.8 km/s and therefore allow it to vary between 5.6 and 6.2 km/s. We allow the low-velocity-layer thickness to vary between 0 and 2,000 m, with the upper limit defined to ensure no points are attempting to exceed it. For each inversion run values are chosen randomly from within these ranges for the starting model. The model is updated by randomly selecting and perturbing one of the parameters. If the selected parameter is the low-velocity-layer thickness, then a section of the layer is chosen to be updated by selecting one of the layer-defining points at random and perturbing it and the points within 5 km. A smoothing function is then applied to reduce unrealistically large variations in the thickness. This filter is applied over 5 km to each side of the point, with weighting of 10, 7, 4, 2 applied at distances of 0, 1, 2.5, 5 km. Various filter lengths and weightings were tested and this combination was found to be optimal to reduce the trade off between over- and under-smoothing.

3.6. Results

The results of the seismic travel-time inversion reveal the low-velocity layer with a maximum thickness of 1.7 ± 0.2 km on the upstream end that thins towards the downstream end of our survey line with a minimum thickness of 115 ± 104 m (Figure 6). The V_p of this layer is 3.12 ± 0.22 km/s and the V_p of the basement rock is 5.87 ± 0.06 km/s. The travel-time residuals between the modeled and observed arrival times have absolute values between 1 and 69.0 ms (Figure 7), with an RMS error of 62.81 ms. The largest travel-time residuals are for the reflection from the base of the low-velocity layer at the downstream receiver array (DS1). The uncertainty of the low-velocity-layer thickness is greater at the upstream end where there were no shots, so only the refracted head wave arrival can be used to constrain the thickness.

We find a low-velocity layer that is thick, in excess of 1,000 m, on the upstream half of our survey line and thins to ∼100 m on the downstream end. The location of the thickest part of this layer on the upstream half of our model roughly corresponds with the sedimentary basin delineated by Jordan et al. (2023) (outlined in orange in Figure 6) and the V_p we obtain is consistent with this being a sedimentary layer. We refer to the material in this layer as sediments but cannot determine what exactly the material is because V_p varies in sediments and sedimentary rocks based on a number of factors that we cannot constrain (Mavko et al., 2020). The thick sediments from ∼25 km to the end of the survey line and the thinning sediment between 10 and 25 km are consistent with the structure of a sedimentary basin, with its downstream edge at ∼10 km distance (gray line in Figure 6). We do not observe the edge or thinning of the sedimentary basin on the upstream end. Downstream of the sedimentary-basin edge at ∼10 km, a thin layer of sediments continues. While we have resolved all the sediments as one layer, which we refer to as the sediment layer, we make a distinction here between the sedimentary basin (10 km onwards) and the sediments outside the sedimentary basin (0–10 km) that is important when discussing the distribution of bed types. Additionally, the higher travel-time misfits on the DS1 indicate there may be some variations in the properties of the layer outside of the sedimentary basin.

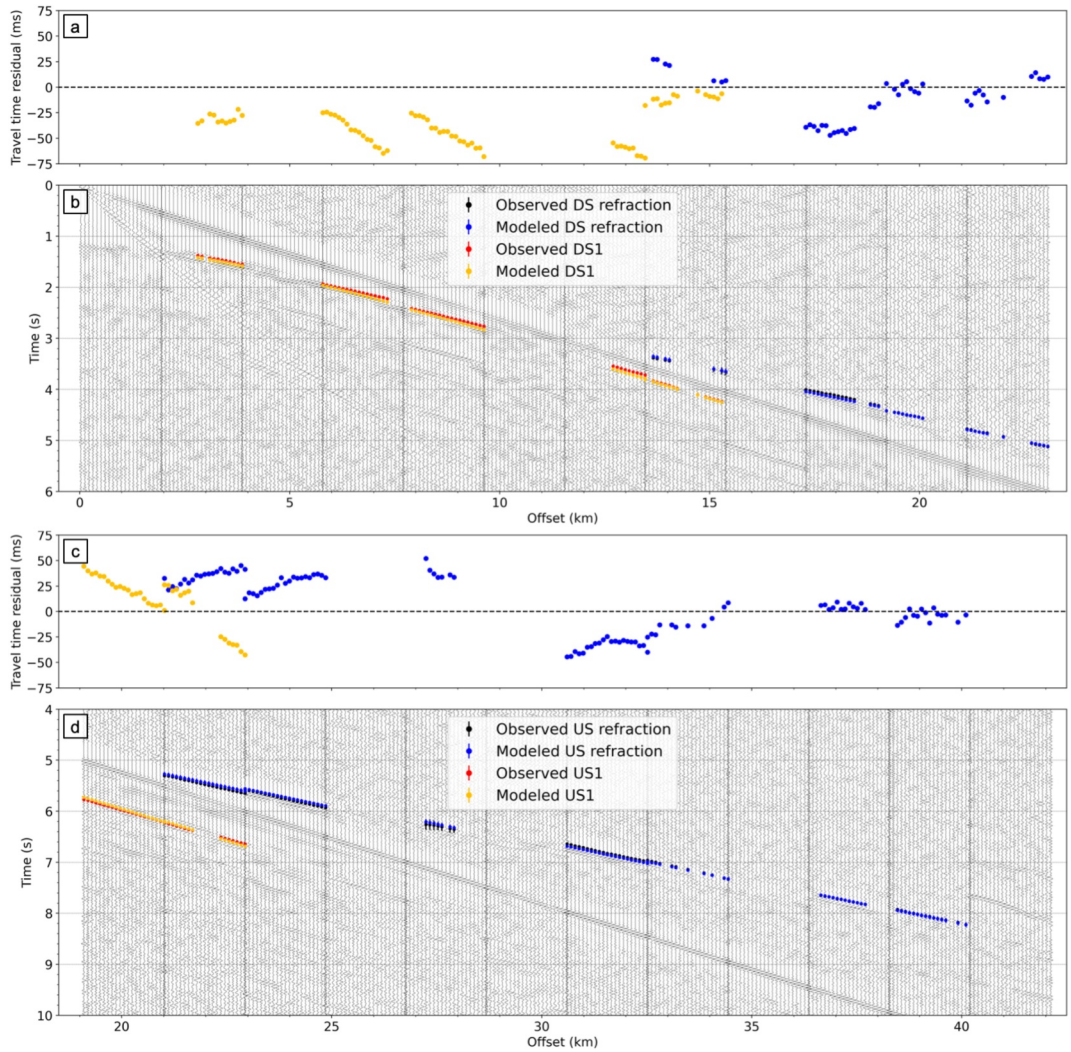

Figure 7. Travel-time residuals and observed and modeled arrivals from the seismic inversion results. (a) Travel-time residuals for refraction and reflection from the low-velocity layer at the downstream array. (b) Observed (picked) and modeled refraction and reflection arrivals. Error bars on the observed points represent the travel-time uncertainty described in Section 3.4. Error bars on the modeled points represent the spread in modeled arrival times across the inversion run. (c) and (d) as (a) and (b) for the upstream receiver array.

4. Potential Fields

We use airborne gravity- and magnetic-anomaly data to extend our investigation of the crustal structures in the along-flow direction and in depth. For our work, we only use the data from the ITGC airborne campaign (Jordan & Robinson, 2021a, 2021b) as it has the highest spatial resolution (shortest resolvable wavelength) of available products (Cochran et al., 2011; Diehl et al., 2008; Jordan & Robinson, 2021a). There is a segment of an airborne-survey line that is coincident with a part of our seismic survey but it only extends for ∼30 km (Airborne Line 3 in Figure 8), which is not long enough to fully capture the wavelength of the signal from the crustal structures. The closest lines that are longer and capture the crustal-structure signals are ∼5 km to the east and west of our seismic survey line (Airborne Lines 1 and 2 in Figure 8). Comparing the data from the short segment with the two continuous lines, we see that there is a high in the gravity and magnetic anomalies at ∼−1,450 to −1,410 km that is persistent across all three airborne lines (Figure 8). Because of the similarity in the shape of the anomalies across all three airborne-survey lines, we use Airborne Lines 1 and 2 that are ∼5 km away, assuming that the modeled sedimentary basin continues to east and west.

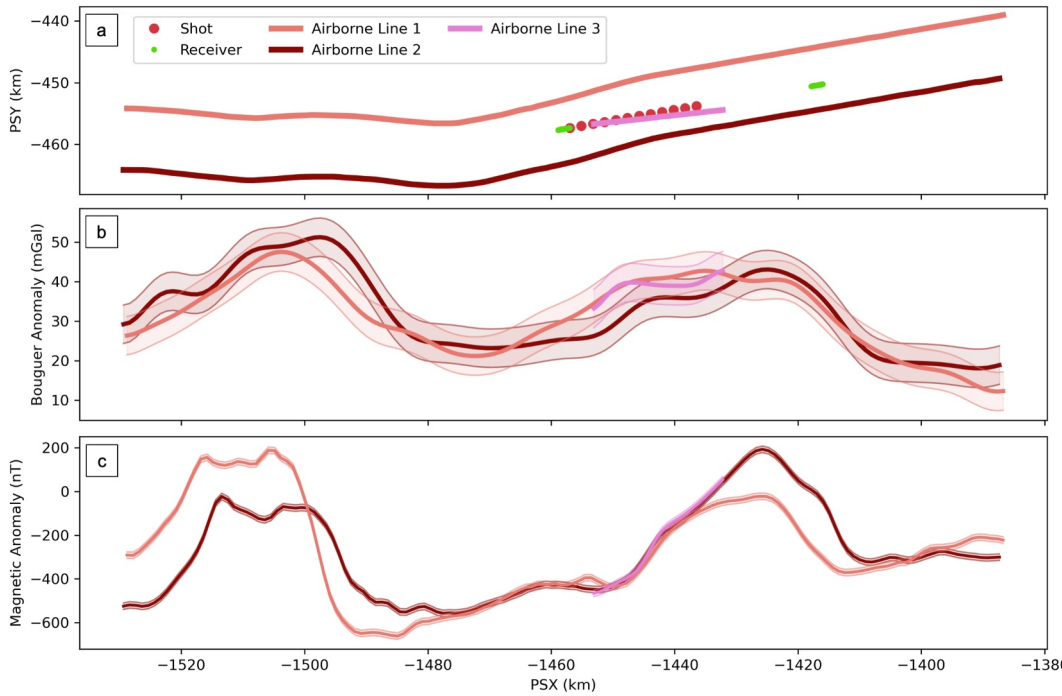

Figure 8. Comparison of airborne gravity- and magnetic-anomaly data with associated uncertainty from the three lines closest to the seismic survey. Data are from the International Thwaites Glacier Collaboration 2019 airborne field campaigns (Jordan et al., 2023; Jordan & Robinson, 2021a, 2021b). PSY = polar stereographic projection *y*-value. PSX = polar stereographic projection *x*-value. (a) Location of the airborne lines and the seismic survey. (b) Airborne gravity-anomaly data for each line with associated uncertainty. (c) Airborne magnetic-anomaly data for each line with associated uncertainty.

As the data are not coincident, we do not attempt a joint inversion of all available data and instead create a forward model to fit the potential-field data. We include the sedimentary layer derived from the seismic travel-time inversion by projecting the thickness onto the potential-field lines. In the seismic data, we do not observe the upstream edge of the modeled sedimentary basin. However, the potential-field lines extend beyond the upstream extent of the seismic survey and therefore we must estimate where this upstream edge is for the potential-field modeling. To do this, we use the bed roughness calculated by Jordan et al. (2023) to assess where the smooth top of the sedimentary basin likely ends (Figure 9). On both Airborne Lines 1 and 2, we place the basin edge where we see an increase in the bed roughness just upstream of where our seismic line ends. We do not have

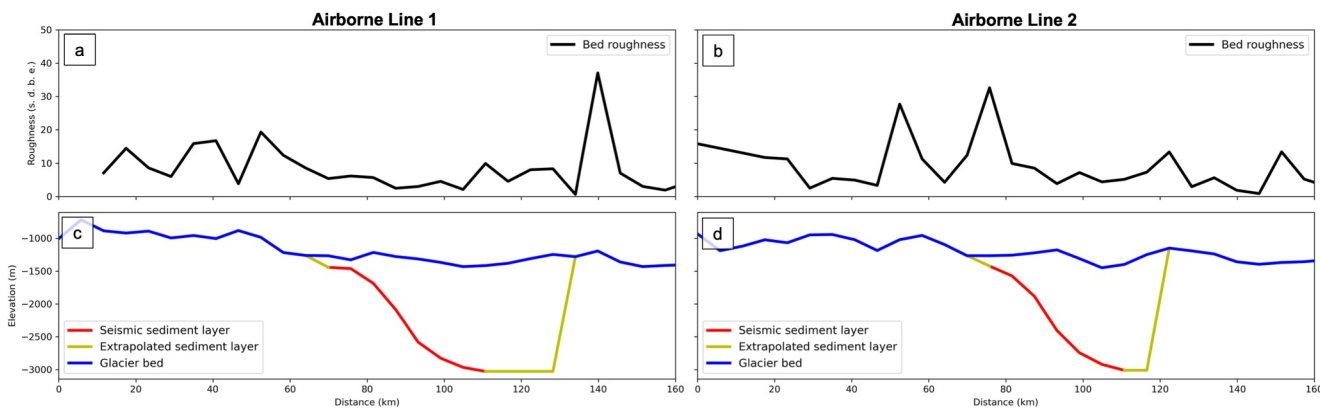

Figure 9. Estimating the upstream edge of the sedimentary basin using bed-roughness data. (a) and (b) show the bed roughness along each airborne-survey line from Jordan et al. (2023), calculated on a 1-km moving window. s. d. b. e. = standard deviation of bed elevation. (c) and (d) show the elevations of the bed, the sediment layer from the seismic results and the extrapolated sedimentary-basin edge based on the bed-roughness data.

sufficient data to justify modeling in 3D, so instead proceed with modeling in 2D, as we have established that the structures extend roughly perpendicular to the airborne-survey lines.

4.1. Data Processing

We obtain the gravity-anomaly data as free-air anomalies that have been corrected for the vertical acceleration during flight, Eötvös effect, latitude and elevation (Jordan & Robinson, 2021a). We interpolate the data to 1-km intervals to reduce computation time in modeling; the minimum resolvable wavelength of the data is ∼5 km and therefore this interpolation will not reduce the size of features that can be detected with the data. We then calculate the Bouguer correction in 3D with elevations from BedMachine and using Fatiando a Terra (Uieda et al., 2013). We correct for the ice (density = 900 kg/m^3) and ocean water (density 1,030 kg/m^3) relative to the basement rock (density = 2,670 kg/m^3) below sea level and to air (density = 0 kg/m^3) above sea level. The Bouguer correction includes wavelengths shorter than those in the free-air anomaly data due to filtering during the processing stages after data collection. To ensure we do not introduce incorrect short wavelength anomalies, we filter both the Bouguer correction and the free-air anomaly with the same low-pass filter with the taper starting at 9 km and cutting off all wavelengths below 5 km. We then sum together the filtered free-air anomaly and Bouguer correction to obtain the Bouguer anomaly.

The magnetic-anomaly data are provided with corrections already applied for the regional geomagnetic field, aircraft motion and diurnal variations (Jordan & Robinson, 2021b). These data are interpolated at the same 1-km intervals as the gravity-anomaly data.

4.2. Uncertainty

The uncertainty of the gravity anomaly data is calculated by taking the root-sum squared of the given uncertainty on the free-air anomaly (1.67 mGal) (Jordan & Robinson, 2021a) and the uncertainty on the Bouguer correction. We calculate the uncertainty on the Bouguer correction by carrying out the correction calculation 100 times, perturbing the bed elevation and the background rock density each time. The bed elevation is perturbed using a normal distribution with the standard deviation equal to the bed-elevation uncertainty and the background rock density is perturbed using a normal distribution with standard deviation of 100 kg/m^3 following Tinto and Bell (2011). The uncertainty of the Bouguer correction is then taken as the standard deviation of the results of the 100 runs, giving a value of 4.55 mGal. The Bouguer-correction uncertainty at each measurement point is then root-sum squared with the uncertainty of the free-air anomaly, giving a mean uncertainty of 4.85 mGal.

We do not perform any additional processing on the magnetic-anomaly data. Therefore, the uncertainty is 14.83 nT, as quoted in the released data set (Jordan & Robinson, 2021b).

4.3. Flexure Modeling

The Bouguer- and magnetic-anomaly data show two positive anomalies at approximately 25 and 100 km distance on both Airborne Lines 1 and 2 (red lines in Figures 10 and 11b–11c). The combination of positive gravity and magnetic anomalies at these locations was interpreted to be caused by mafic bodies by Jordan et al. (2023). However, the positive anomaly at ∼100 km overlies the sedimentary basin which produces a modeled negative anomaly with maximum amplitude of −26 mGal on Airborne Line 1 and -23 mGal on Airborne Line 2. In the Ross Sea, Karner et al. (2005) showed that a similar observation of gravity-anomaly highs over sedimentary basins was not due to crustal intrusions and instead was due to varying flexural strength of the lithosphere between the time of the opening of the basin and filling it with sediments. We investigate the origin of this gravity-anomaly signal with flexural modeling at our study site. We follow the processes-orientated approach first outlined by Watts (1988) to reconstruct and model the flexure at the base of the crust at different points through the history of its formation.

Flexural modeling requires the flexural strength of the lithosphere to be defined in terms of the elastic crustal thickness (T_e). A higher T_e value indicates stronger crust that will distribute a load over a larger area and for $T_e = 0$ (Airy isostasy) all loads cause variations in the crustal thickness only directly underneath them (Watts, 2023). We model the scenario of varying T_e outlined by Karner et al. (2005) with Airy isostasy for processes that occurred during rifting, when the crust likely has a low T_e value (Watts & Burov, 2003), and $T_e = 20$ km for processes that occurred after rifting, approximately the current estimated value in our study

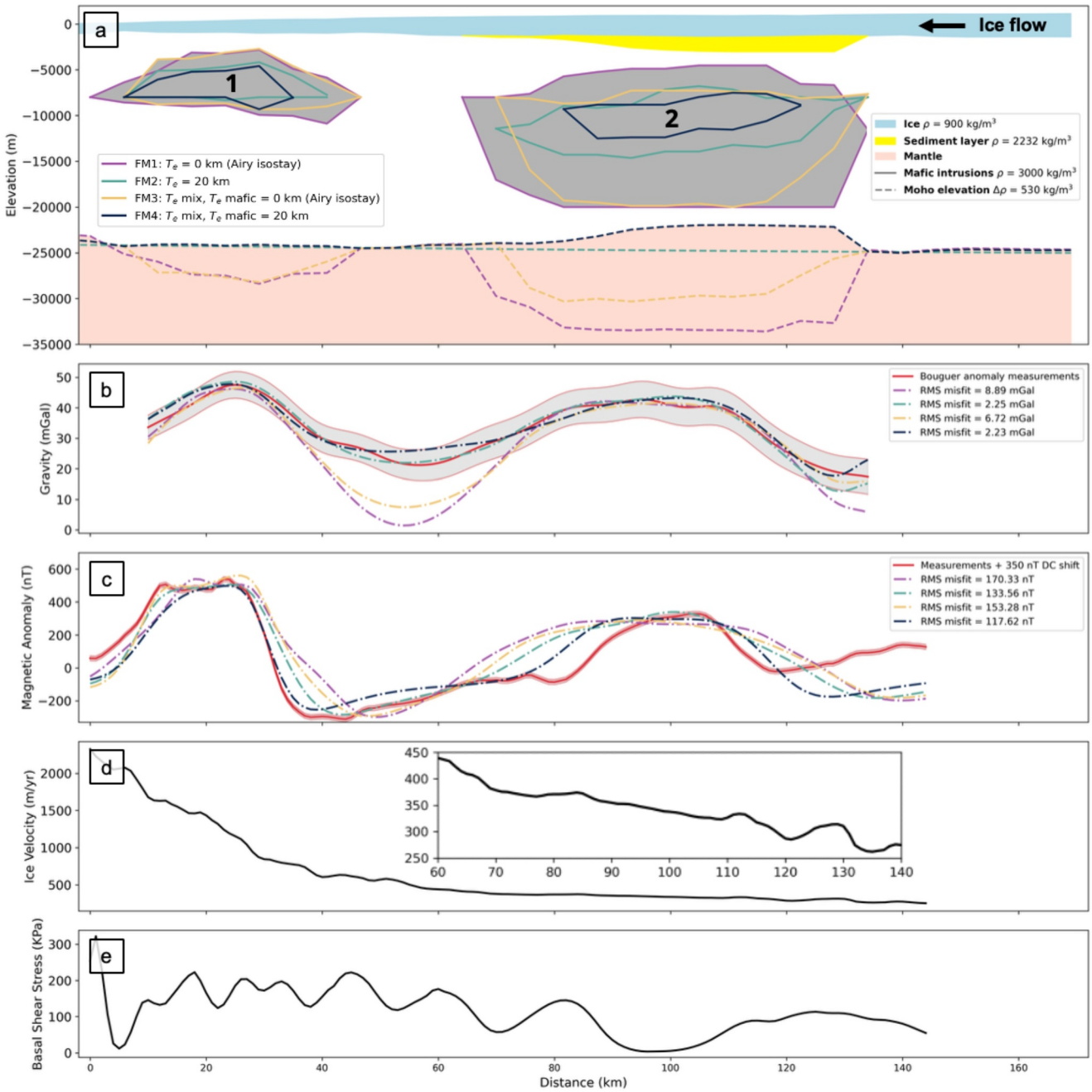

Figure 10. Modeling results from Airborne Line 1 with ice-flow velocity and modeled basal shear stress. (a) Crustal structures with sediment layer from seismic measurements in yellow and mafic intrusions numbered 1 and 2. Results from four different flexural modeling scenarios (described in main text) are shown with varying size of mafic intrusions and Moho depth. (b) Bouguer gravity anomaly data and results for each of the flexural modeling scenarios with associated RMS error. (c) Magnetic anomaly data and results for each of the flexural modeling scenarios with associated RMS error. (d) Ice-flow velocity from Mouginot et al. (2019) interpolated along Airbone Line 1. The inset is zoomed in between 60 and 140 km and with a different scale for the velocity. (e) Basal shear stress from McCormack et al. (2022) interpolated along Airbone Line 1.

area (Swain & Kirby, 2021). This scenario is named T_e *mix*. We additionally model the two end-member scenarios for Airy isostasy or T_e = 20 km at all times. Throughout our flexural modeling, we use Young's Modulus of 1×10^{11} Pa and Poisson's ratio of 0.25. For the densities of the model components, we use background crustal density of 2,670 kg/m^3, ice density of 900 kg/m^3 and sediment density of 2,232 kg/m^3, based on the seismically derived V_p of 3.04 km/s and the velocity-density relationship of Brocher (2005). We

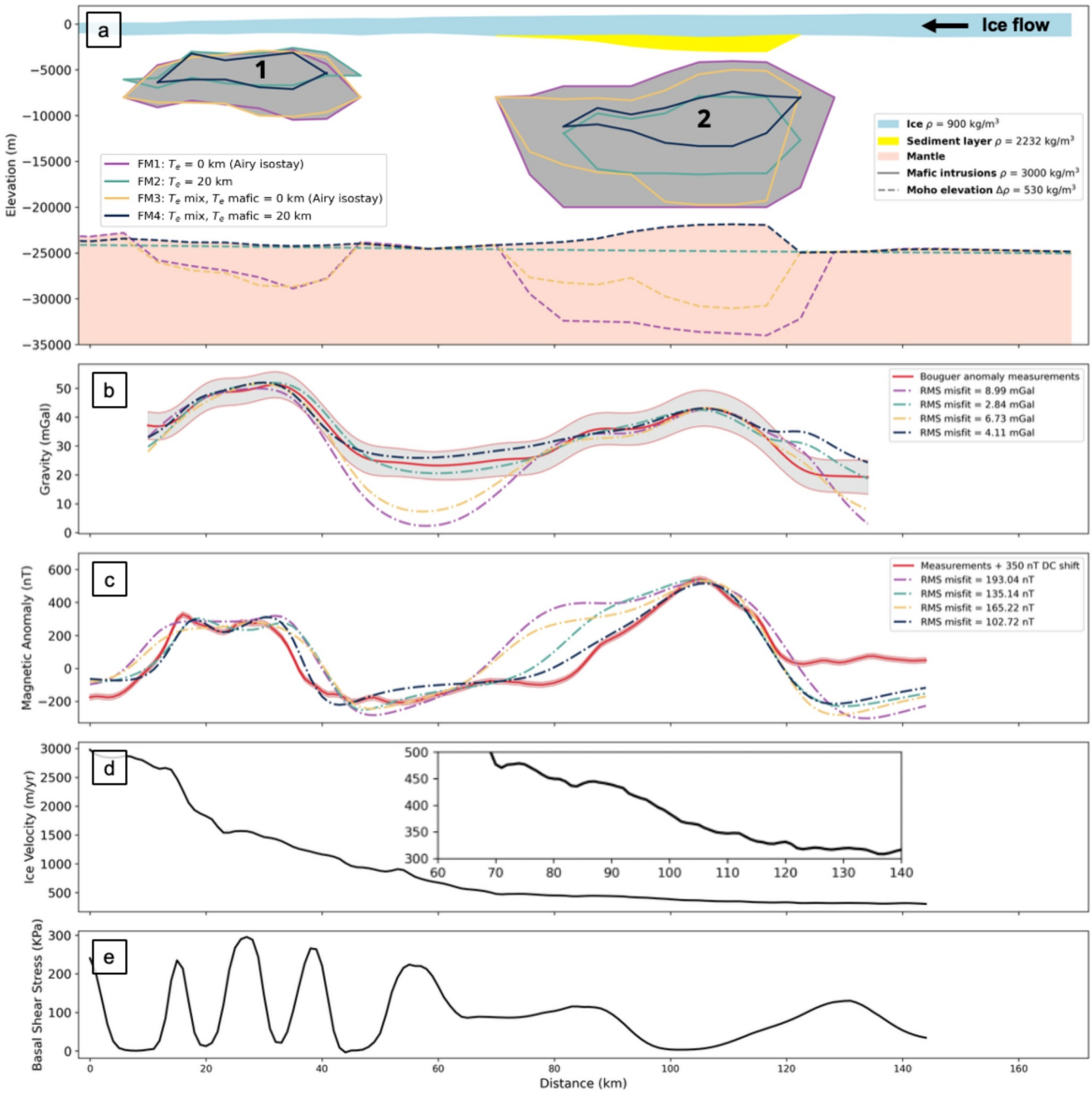

Figure 11. Modeling results from Airborne Line 2 with ice-flow velocity and modeled basal shear stress. See Figure 10 caption.

use a lower crustal density of 2,800 kg/m^3 (Damiani et al., 2014) and a mantle density of 3,330 kg/m^3, giving a density contrast at the Moho of 530 kg/m^3. Variations in this density contrast will cause changes in the absolute value of the Moho flexure but not its wavelength, as discussed in Jordan et al. (2010).

In the following we summarize the steps in the process-orientated gravity modeling as applied to our model, for further details on the process see Watts (2023). For the T_e *mix* scenario the value of T_e used at each step is given, and for the Airy isostasy and $T_e = 20$ km scenarios T_e is held constant at all steps. The first step is to backstrip the load of the sediment to find the basin topography at the time of its formation. We use the seismically derived sediment layer thickness and for the T_e *mix* model, assign $T_e = 20$ km, assuming that sediment deposition would have occurred after rifting when the lithospheric strength had increased. Next, we calculate the flexure due to the

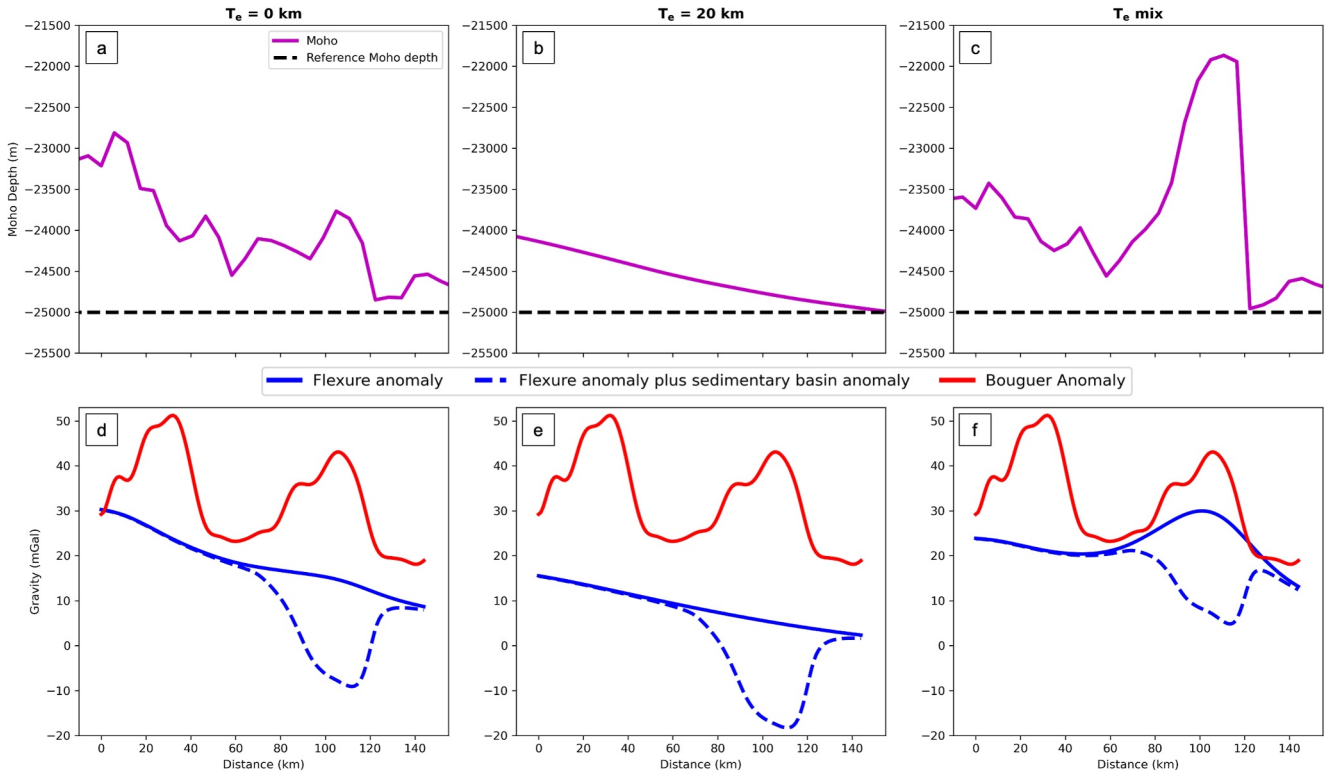

Figure 12. Results from flexural modeling on Airborne Line 2. (a), (b) and (c) show the Moho depth from each of the modeled scenarios described in the text, with relevant scenario titled above each panel. (d), (e) and (f) show the resulting Bouguer anomalies for Moho depth relative to the reference Moho depth in each of the modeled scenarios.

topography before ice loading. For this, we used the rebounded bed topography (Paxman et al., 2022) and assume that all areas below sea level are covered with ocean water. We make this calculation in 3D to account for the topography off the survey lines and then interpolate the 3D calculation onto the survey lines. We also include the flexure due to the backstripped basin topography, again assuming that it is filled with ocean water at this time. For the T_e *mix* scenario, we assume that the topography would have been formed before or during rifting and therefore assign Airy isostasy. Once the basin topography has been formed, it will be filled with sediment, creating the load that we removed in the backstripping in the first step. Therefore, we add back in this load, as stated previously for the T_e *mix* scenario we are assuming this loading occurred after rifting when the lithospheric strength had increased and therefore that $T_e = 20$ km. The final step is to add the flexure from the ice load. We calculate this using the ice thickness from BedMachine in 3D and interpolate along the survey lines. For the T_e *mix* scenario, we again assume ice loading occurred after rifting and assign $T_e = 20$ km. The flexure from each of these contributions is summed together to give the total flexure at the base of the crust, with positive values indicating a flexure upwards towards the surface and negative flexure indicating flexure downwards away from the surface.

The total flexure is then added to the reference crustal thickness. We use 25 km as this reference crustal thickness because it is representative of crustal-thickness estimates by several previous studies in the Thwaites Glacier area (Damiani et al., 2014; Jordan et al., 2020; Ramirez et al., 2016; Winberry & Anandakrishnan, 2004) that range between 20 and 29 km. We calculate the gravity anomaly due to this flexure in 2D, with a positive anomaly where the crust is flexed upwards and negative anomaly where it is flexed downwards, relative to the reference crustal thickness. Our 2D calculation here and throughout this work uses the line-integral method of Won and Bevis (1987), implemented in pyGIMLi (Rücker et al., 2017).

This initial flexural modeling gives results for each of the Airy isostasy, $T_e = 20$ km and T_e *mix* scenarios (Figure 12). The Airy isostasy scenario gives an undulating Moho as expected because each load is compensated directly below itself. Conversely, the $T_e = 20$ km scenario shows a smoothly varying Moho due to the increased flexural strength, causing loads to be distributed over a larger area. Both of these scenarios show no evidence of

Table 3
Magnetic Susceptibilities Used in Mafic-Intrusion Modeling

		Airborne line 1		Airborne line 2	
Flexure modeling scenario	Scenario number	Body 1	Body 2	Body 1	Body 2
T_e = 0 km	FM1	100	50	70	70
T_e = 20 km	FM2	170	100	90	130
T_e *mix*, T_e mafic = 0 km	FM3	110	60	60	80
T_e *mix*, T_e mafic = 20 km	FM4	170	150	100	170

Note. All values are susceptibility contrast to the basement rock and are given in 10^{-3} SI units.

the sedimentary-basin topography because the same value of T_e has been used during rifting and sedimentation. In contrast, the T_e *mix* scenario shows a large upwards flexure in the Moho at the location of the sedimentary basin due to the lower T_e during rifting compared with sedimentation. The gravity anomalies from the scenarios are shown below the Moho elevations. The Airy isostasy and $Te = 20$ km scenarios show similar results, with Airy isostasy having a larger gravity anomaly due to the greater upward flexure. The T_e *mix* scenario shows a positive anomaly where the Moho is flexed upwards under the sedimentary basin. However, when combined with the negative anomaly from the sedimentary basin, this positive anomaly reduces to an anomaly with a negative trend. This demonstrates that variations in T_e alone cannot explain the positive anomaly in the gravity data and additional structures in the crust must be added. As discussed by Jordan et al. (2023), these structures are causing a gravity- and magnetic-anomaly high and are therefore likely mafic intrusions. We continue with this interpretation and include mafic bodies with positive density and magnetic-susceptibility contrasts in our model.

4.4. Mafic Intrusions

We create a forward model for each of the potential-field lines, including the sediment thickness, mafic intrusions and variation in crustal thickness due to isostatic compensation. For the model on each line, we calculate the gravity and magnetic anomalies in 2D. For the gravity anomaly, we again model scenarios with Airy isostasy (FM1) and $T_e = 20$ km (FM2) at all times, now also including mafic intrusions. For the T_e *mix* scenario, we model two variations, one where the mafic intrusions formed during rifting and are compensated with Airy isostasy (FM3), and one where they formed after rifting and are compensated with T_e = 20 km (FM4). The magnetic anomaly is calculated using the line-integral method of Won and Bevis (1987), implemented in pyMag2Dpoly (Ghirotto et al., 2021). The field strength, inclination and declination at our study site are derived from the International Geomagnetic Reference Field (Alken et al., 2021). We model the mafic intrusions with a density of 3,000 kg/m^3 and variable magnetic susceptibility (Table 3). We use the same density value as modeled for similar mafic intrusions offshore of Thwaites Glacier by Kalberg et al. (2015).

The forward model of the mafic bodies is manually perturbed for each T_e scenario separately to reduce the misfit between the modeled and measured gravity and magnetic anomalies. Obtaining a suitable fit between the model and the measurements for both the gravity- and magnetic-anomaly data gives some indication of the depth of the bodies. However, there is still a trade off between the depth, size and properties of the bodies that makes it difficult to determine where in the crust they lie.

4.5. Results

We model two mafic bodies at 25 and 100 km distance on Airborne Lines 1 and 2 (Figures 10 and 11). The RMS misfit varies with the flexure-modeling scenario. FM1 and FM3 both have a high RMS misfit with the gravity-anomaly data because the modeled anomaly is too low at ∼50–70 km. This is due to the downward flexure of the Moho under the mafic intrusions in these scenarios that causes a negative gravity contribution. This downward Moho flexure also results in larger mafic bodies in these scenarios in order to fit the data. This is especially evident for Body 2, which, on Airborne Line 1, has a maximum thickness of 15.5 km for FM1 and 12.6 km for FM3. In comparison, this body has a maximum thickness of 7.1 km in FM2 and a maximum thickness of 4.1 km in FM4. The depth of Body 2 also varies with the Airy isostasy scenario resulting in a body at ∼5-km deep and other scenarios finding the body at ∼10-km deep. Similar values for maximum thickness and depth are seen on Airborne Line 2. The greater thickness and length of Body 2 modeled for the Airy isostasy scenarios results in a

modeled magnetic anomaly that is wider than that seen in the data. This results in the Airy isostasy scenarios, FM1 and FM3, having a higher RMS error for the magnetic-anomaly data than those with $T_e = 20$ km, FM2 and FM4.

Body 1 has a smaller variation in maximum thickness with a range of ∼3.5 km across all scenarios and is consistently ∼4-km deep. We do not have any additional measurements to constrain the depth of this body but the shape of the anomaly with the double high indicates it is closer to the surface than Body 2. While we have modeled Body 2 to be at approximately the same depth across all the scenarios, there is a possibility of more variable depth and thickness than we show here.

5. Discussion

5.1. Crustal Structures

We model a sedimentary basin with maximum thickness of 1.7 ± 0.2 km and a layer of sediment 100- to 300-m thick outside of the sedimentary basin (Figure 6). There are no other active-seismic-based estimates of the sediment thickness below Thwaites Glacier. There are multiple estimates based on passive-seismic methods but these methods have a coarser resolution that limits the ability to model individual sedimentary basins; hence we have no direct comparisons of sediment thickness in our study area. However, passive-seismic estimates do indicate sedimentary-basin thicknesses of 900–1,500 m elsewhere on Thwaites Glacier (Dunham et al., 2020; Zhou et al., 2022) and a sedimentary-basin thickness of 1,200 m is estimated beneath neighboring Pine Island Glacier based on reflection-seismic and gravity- and magnetic-anomaly data (Smith et al., 2013). Our results are comparable to these previous works conducted in the ASE, indicating our sediment thickness estimates augment the current knowledge of sedimentary-basin thickness beneath Thwaites Glacier.

We make a distinction in our results between the sedimentary basin and the sediment cover outside of the basin. The basin is at the same location as a sedimentary basin outlined in horizontal extent by Jordan et al. (2023). At the downstream end, we model the basin pinching out between 10 and 25 km distance (Figure 6). The downstream boundary of the basin is not clearly defined but it is likely at around 10 km distance along our profile, whereas the boundary of the basin drawn by Jordan et al. (2023) where it intersects our survey line is further upstream at 18 km distance. The basin extends at least to the upstream extent of our data. This is beyond the upstream basin boundary drawn by Jordan et al. (2023), which ends ∼8 km downstream of the extent of our data. We have therefore revealed that the sedimentary basin is wider in the along-ice-flow direction along our survey line than previously estimated.

As explained in Section 5, we do not image the upstream edge of this sedimentary basin but we infer the basin to continue about 5–15 km farther upstream to an area with higher and rougher bed topography, or 'highlands' revealed by Clyne et al. (2020) (Figure 9). Based on knowledge of regional geology and on the sharp contrast in topography and lithology, we suggest that there is a fault striking across ice flow that separates this upstream end of the basin from the upthrown basement block that forms the highlands. The downstream end of the basin thins more gradually, suggesting that the basin is a half-graben (Figure 2).

In addition to the sedimentary basin, we have also modeled two mafic intrusions. These had previously been suggested by Jordan et al. (2023) but we provide the first estimate of their depth and thickness by including the sedimentary basin and considering the crustal flexure. During modeling with gravity data, we consider scenarios with varying flexural strength of the crust, which results in varying size of the mafic bodies (Figures 10 and 11). The Airy isostasy scenarios (FM1 and FM3) produce results with higher RMS misfits for both the gravity- and magnetic-anomaly data. The poorer fits indicate that the mafic intrusions are unlikely to have been compensated with Airy isostasy. However, FM4 has a period of Airy isostasy during rifting processes and obtains a better fit with the data. This indicates that there may have been low flexural strength at some point during the tectonic history of the lower part of Thwaites Glacier. We take FM2 and FM4 to be the likely scenarios based on our modeling and therefore estimate the maximum thickness of the mafic intrusions to vary between 3.8 and 8.6 km.

Our preferred flexural-modeling scenarios (FM2 and FM4) have gravity-anomalies that result in RMS misfit less than the mean uncertainty on the Bouguer-anomaly data of 4.85 mGal. This demonstrates a good fit within the data uncertainty, despite the model results deviating from uncertainty bands on the data at some points. The magnetic-anomaly results from these scenarios have RMS misfits much larger than the quoted uncertainty on the data of 14.83 nT. The larger misfits on the magnetic-anomaly data are likely due to various other factors that may be affecting the data, including remanent magnetism, the orientation of subsurface bodies and variations in

magnetic properties of the basement rock. We partially account for these other factors by applying a DC shift to the data to align it with signal from our modeling. We additionally allow the magnetic susceptibility to vary between model scenarios for each of the mafic bodies to obtain the best fit for both the gravity and magnetic anomaly data. To better constrain the depth, thickness and properties of these mafic bodies, more data, such as active seismic with a stronger source or magnetotelluric measurements (Killingbeck et al., 2024), are needed.

5.2. Formation of the Crustal Structures

Our model of the crustal structures gives insight into the possible origin of these structures and the tectonic history in the Thwaites Glacier region. It is unusual to observe a positive gravity anomaly over a sedimentary basin as the negative density contrast of the sediment infill compared to the basement rock on its own creates a negative gravity anomaly. As discussed in Section 4.3, positive gravity anomalies over sedimentary basins have also been observed in the Ross Sea and explained by a variation in the flexural strength of the lithosphere between the time of the basin formation and sediment infill (Karner et al., 2005). However, as outlined in Karner et al. (2005) and shown through our modeling, the sedimentary basin we have modeled is below the minimum size required for variation in the flexural strength of the lithosphere to be the explanation for the positive gravity anomaly. There is evidence of positive gravity anomalies over sedimentary basins caused by mafic intrusions within rift systems in other locations. One example is the Kenya Rift, where mafic intrusions have been inferred within the rift system from high *P*-wave velocities (Keller et al., 1994; Prodehl et al., 1994) and positive gravity anomalies (Sippel et al., 2017). These intrusions are generally at less than 10-km deep, ∼5-km thick and 20-to 50-km wide. These are similar to the mafic intrusions we have modeled, although the intrusions in the Kenya Rift appear to be associated with a thicker sediment layer with a maximum thickness of greater than 10 km locally (Sippel et al., 2017). This shows the mafic intrusions in the Kenya Rift may not be at the same location within the rift system as the structures we find. However, regardless of location and size, mafic intrusions within rift systems are commonly linked to upwelling of magma due to crustal thinning during rifting (e.g., Sandrin & Thybo, 2008; Swain et al., 1994).

Mafic intrusions similar to those we have modeled have been observed offshore of Thwaites Glacier by Kalberg et al. (2015). They modeled intrusions ∼5- to 15-km thick and the authors relate these to the gabbro of the Dorrel rock intrusive complex in Marie Byrd Land (Rocchi et al., 2006), which is dated to be emplaced during the late Cenozoic phase of rifting around 34 Ma. Our mafic intrusions could be of a similar origin to those offshore. However, Jordan et al. (2023) discuss the origin of mafic intrusions under Thwaites Glacier that correspond to the ones we have modeled and prefer an explanation of formation during an earlier period of rifting in the Cretaceous. Elsewhere in the WARS, strong magnetic anomalies related to mafic intrusions have also been observed at Marie Byrd Land (Ferraccioli et al., 2002) and at the rift flank in the Transantarctic Mountains (Ferraccioli et al., 2009), where their formation was related to rifting in the Eocene to Oligocene. We have little evidence to determine the origin of the mafic intrusions we have modeled without additional data, for example, from geochemical dating of samples. However, it is likely they were formed in a rift-related setting during the late Cenozoic, as has been suggested for other large mafic intrusions in the region.

Offshore of Thwaites Glacier, Kalberg and Gohl (2014); Kalberg et al. (2015) also imaged horst and graben, and fault-like structures with marine reflection-seismic data, which they interpreted as sedimentary basins that formed during a period of rifting in the Cretaceous. The sedimentary basins they find are between 20- and 100-km wide and 0.7- to 1.5-km thick, with *P*-wave velocities between 1.7 and 3 km/s. The sedimentary basin we imaged is comparable in width to the smaller of these basins and similar in thickness. Under Thwaites Glacier, LeMasurier (2008) interpreted the existence of rift formed basins with no thick sediment fill to suggest that these basins were formed during rifting in the Neogene, with insufficient time for sediment infill to have occurred. It is unclear at this point if the sedimentary basin we modeled is also formed during rifting in the Neogene, or during an earlier phase of rifting in the Cretaceous.

5.3. Influence on Glacier Dynamics

Our model shows a variation in crustal structures along the direction of ice flow on the main trunk of Thwaites Glacier. The sedimentary basin we model lies within an area of smooth, low-lying topography. Although not coincident with our seismic line, Clyne et al. (2020) found continuous soft bed within the same smooth, low-lying area of Lower Thwaites (Figure 2), indicating that this area of continuous soft bed is likely the top of the

sedimentary basin we have modeled. Regions with smooth, low-lying topography, or 'lowlands', with continuous soft bed such as this are identified at both Lower Thwaites (Clyne et al., 2020) and Upper Thwaites (Muto et al., 2019). Our results thus indicate that these lowlands are the likely locations of sedimentary basins with continuous soft bed under Thwaites Glacier.

Sedimentary basins can influence the dynamics of overlying ice by being a source of deformable sediments and water. Sediments at the ice-bed interface can allow rapid ice flow by soft-bed slip, a combination of the deformation within sediments and sliding of ice along the top of them (Cuffey & Paterson, 2010; Zoet & Iverson, 2020). Sediments deform when the subglacial water pressure is sufficiently high to lower the yield strength of the sediments and the applied shear stress exceeds this yield strength (Cuffey & Paterson, 2010). When the subglacial water pressure is close or nearly equal to the ice-overburden pressure, basal contact and hence the drag is reduced, sometimes close to flotation, accommodating high sliding velocity (Engelhardt & Kamb, 1998; Kamb, 2001). Sedimentary basins can control the subglacial water pressure at and near the bed as they may store groundwater or release it into the subglacial hydrological system with fluctuations in the ice mass above (Christoffersen et al., 2014; Siegert et al., 2018). The movement of water through the sedimentary basin can also advect geothermal heat at the base of the sedimentary basin to the ice-bed interface (Gooch et al., 2016). Increased heat flow to the glacier bed may lead to additional melt and therefore could also increase the subglacial water pressure.

Downstream of the sedimentary basin, the bed topography becomes rougher and the sediment thickness reduces but is still at least ca. 100 m. Higher relief areas like this have been found to have alternating soft bed and hard bed at Upper Thwaites (Muto et al., 2019) and Lower Thwaites (Clyne et al., 2020). However, initial results from reflection seismic data collected over the downstream 15 km of our survey line indicate sediment cover over this rougher terrain (Agnew et al., 2025). The sedimentary basin we identify in this study is likely the source of these sediments.

At our study site, we observe the ice flow across a rift-formed sedimentary basin. The sedimentary basin is consistent with the geologic bodies mapped by Jordan et al. (2023), which are shown to be oriented nearly orthogonal to the direction of the ice flow. These observations demonstrate that Thwaites Glacier flows across geologic boundaries rather than being confined by them as other fast-flowing glaciers and ice streams in West Antarctica are (Anandakrishnan et al., 1998; Bell et al., 1998; Bingham et al., 2012; Peters et al., 2006; Smith et al., 2013). Ice-flow velocity across the sedimentary basin increases slightly, from ∼310 m/year to ∼370 m/year along Airborne Line 1 and from ∼300 m/year to ∼310 m/year, but this is within the general trend of velocity increase from inland towards the coast (Figures 10d and 11d). This mainly reflects the thinning of the glacier and the steepening of the glacier surface towards the coast and the consequent increase in the driving stress, and not necessarily the existence of the sedimentary basin and inferred transitions in the bed type. On the other hand, modeled basal shear stress (McCormack et al., 2022) shows the longest stretch of low values within our study area over the sedimentary basin (Figures 10e and 11e). Boundaries of the sedimentary basin and transitions in basal shear stress do not match exactly and large fluctuations in basal shear stress with equally low values are seen farther downstream. However, the approximate co-location of the sedimentary basin and the areas of sustained low basal shear stress indicates the influence of the tectonic structures on bed-type variability that dictates the slipperiness of the glacier bed, supporting a previous suggestion of Jordan et al. (2023) that the geological template of the past rifting directly influences the flow of Thwaites Glacier.

Glacier-evolution modeling has shown that these across-flow geologic boundaries and resulting bed-type distribution beneath Thwaites Glacier can lead to different retreat rates and sea-level contributions. In forced grounding-line-retreat simulations, Thwaites Glacier retreated faster with the simulated uniform hard bed than with uniform soft bed (Parizek et al., 2013; Schwans et al., 2023). However, simulations with alternating soft and hard bed showed retreat behaviors that depart from either of the uniform-bed-type cases (Koellner et al., 2019).

The mafic intrusions we model are not at the ice-bed interface, so they will not directly influence the ice flow. However, their location in the crust and thickness demonstrate heterogeneity in the composition of the crust in our study area. Crustal composition influences the radiogenic heat production, which will then affect the magnitude of the heat flow at the glacier bed (Burton-Johnson et al., 2020; Carson et al., 2014), having implications for melting and water availability at the bed. Within the crust, the upper crust has been shown to have the greatest influence on the geothermal flow at the surface, contributing 26%–40% of total continental heat flow (Artemieva & Mooney, 2001; Burton-Johnson et al., 2020; Pollack & Chapman, 1977; Vitorello & Pollack, 1980). Most heat

production in the crust comes from heat-producing elements (Beardsmore & Cull, 2001), which are more compatible in the minerals of silicic rocks than mafic rocks; hence mafic rocks produce less heat (Slagstad, 2008). Due to limited knowledge of the crustal composition, most estimates of the heat flow in Antarctica assume a homogeneous crust with constant heat production in each of the lower, mid and upper crust (e.g., An et al., 2015), or do not include crustal heat production due to lack of constraints (e.g., Dziadek et al., 2021). Our model resolves the downstream mafic intrusion within the upper to mid crust at ∼5 km depth and the upstream intrusion in the mid crust at ∼10 km depth. These large mafic bodies with lower heat production may be acting to lower the heat flow compared to neighboring areas, although this cannot be confirmed without any geochemical analysis or direct observations of the heat flow. While the impact of these intrusions on current ice dynamics is still unclear, estimating their likely thickness and depth improves the understanding of the amount of mafic magmatism that occurred during formation of the WARS.

6. Conclusion

We have modeled crustal structures under a lower part of Thwaites Glacier in West Antarctica using long-offset seismic, and gravity- and magnetic-anomaly data along two ∼120-km-long lines roughly parallel to the ice flow. With the travel times from arrivals in the seismic data, we modeled a sedimentary basin at the upstream end of our study area. This sedimentary basin is ∼40-km long and has a maximum thickness of 1.7 ± 0.2 km. The potential-field data show positive gravity and magnetic anomalies over this sedimentary basin and an additional positive anomaly ∼80 km downstream. We test and rule out that the positive anomaly over the sedimentary basin is due to varying flexural strength of the lithosphere during the basin formation. We instead fit the potential-field data by including two mafic intrusions with positive density and magnetic-susceptibility contrasts with the basement rock. We model the shape of these mafic intrusions under four flexural-modeling scenarios and determine that they are likely isostatically compensated with a flexural lithosphere strength greater than Airy isostasy. Our preferred scenarios give maximum thickness between 3.8–4.7 km for Body 1 and 4.1–8.6 for Body 2.

The crustal structures we have modeled are similar to those that have been identified offshore of Thwaites Glacier and likely originate from the rifting associated with the WARS in either the Cretaceous or the late Cenozoic epoch. The sedimentary basin lies within the same area of smooth, low-lying topography with continuous soft bed that was found with a previous reflection-seismic survey. This suggests that such bed-topographic characteristics are associated with sedimentary basins elsewhere under Thwaites Glacier. Our modeling also shows a layer of sediments ∼100–300 m thick downstream of the sedimentary basin. We suggest that the rift-formed sedimentary basin is a source of deformable sediments and subglacial water, which are both requisite for soft-bed slip that is likely occurring in our study area. The flow of ice across the edge of the sedimentary basin demonstrates that Thwaites Glacier is flowing across a tectonic boundary. This agrees with previous work showing the tectonic structures under Thwaites Glacier are oriented nearly perpendicular to the direction of ice flow (Jordan et al., 2023). The variable bed-type distribution and the glacier flow across them has been shown to influence the future retreat and sea-level contribution of Thwaites Glacier (Koellner et al., 2019). Our results thus indicate that tectonics and resulting crustal structures influence the behavior of Thwaites Glacier.

Further work on Thwaites Glacier would improve our understanding of the tectonic history and resulting crustal structures, and their relation to ice flow. This could be achieved effectively with more ground-based geophysical data. More spatially distributed long-offset seismic surveys would allow further mapping of upper-crustal structures, and longer survey lines and larger shots would enable imaging of deeper structures and determination of crustal thickness. Magnetotelluric measurements would help constrain mid- to lower-crustal structures, especially mafic bodies. Such ground-based surveys coupled with airborne swath-radar and potential-field data would extend our detailed view of the glacier bed and the crust beneath it. As our study is limited to the lower part and along the main trunk of Thwaites Glacier, surveys further upstream and towards the glacier margins or into tributaries are desirable. Some of these were conducted as part of recent field work of ITGC GHOST and Thwaites Interdisciplinary Margin Evolution projects and results are forthcoming. Future work should involve further mapping of crustal structures and testing of their relation to the ice flow, and investigate how such knowledge could be effectively incorporated into ice-sheet models to improve the prediction of future Thwaites Glacier and the WAIS evolution.

Conflict of Interest

The authors declare no conflicts of interest relevant to this study.

Data Availability Statement

Segy files from the seismic survey (Borthwick et al., 2025c), results of the travel-time inversion and forward modeling (Borthwick et al., 2025b) and codes used for the travel-time inversion (Borthwick et al., 2025d) and flexural modeling (Borthwick et al., 2025a) are available.

Acknowledgments

We thank all members of the 2023-24 GHOST field team, US Antarctic Program staff at WAIS Divide, members of the Air National Guard 109th Air Wing and British Antarctic Survey Twin Otter crew for facilitating and assisting in the collection of the data. Special thanks to the field guide Catrin Thomas, and Tanner Kuhl and Barb Birrittella from the NSF Ice Drilling Program. We thank Fausto Ferraccioli and an anonymous reviewer for their constructive reviews that improved the manuscript. This work was supported by NSF under grant PLR-1738934, OPP-2001714 and OPP-2002346, and NERC under grant NE/S006672/1. Reference Elevation Model of Antarctic surface elevations were provided by University of Minnesota Polar Geospatial Center. This work is from the Geophysical Habitat of Subglacial Thwaites (GHOST) project, a component of the International Thwaites Glacier Collaboration (ITGC). Members of the ITGC GHOST team are Rob Arthern, Robert Bingham, Julien Bodart, Elizabeth Case, Knut Christianson, Olaf Eisen, Kevin Hank, Andrew Hoffman, Coen Hofstede, Nick Holschuh, Jonny Kingslake, Felipe Napoleoni, Helen Ockenden, Rebecca Pearce, Byron R. Parizek, Kiya Riverman, Emily Schwans, Andy Smith, Leigh Sterns, Nathan Stevens, Paul Winberry, Jaiden Zak, Ole Zeising, and Luke Zoet. ITGC contribution No. ITGC-152.

References

Agnew, R., Brisbourne, A., Anandakrishnan, S., Muto, A., Borthwick, L., Willet, A., et al. (2025). Seismic reflection surveys at GHOST Ridge, Thwaites Glacier. In *Abstract EGU25-12160. Paper presented at the EGU general assembly 2025 abstracts*.

Alken, P., Thébault, E., Beggan, C. D., Amit, H., Aubert, J., Baerenzung, J., et al. (2021). International geomagnetic reference field: The thirteenth generation. *Earth Planets and Space*, *73*(1), 49. https://doi.org/10.1186/s40623-020-01288-x

Alley, R. B., Holschuh, N., Parizek, B., Zoet, L. K., Riverman, K., Muto, A., et al. (2022). GHOSTly flute music: Drumlins, moats and the bed of Thwaites Glacier. *Annals of Glaciology*, *63*(87–89), 153–157. https://doi.org/10.1017/aog.2023.43

An, M., Wiens, D. A., Zhao, Y., Feng, M., Nyblade, A., Kanao, M., et al. (2015). Temperature, lithosphere-asthenosphere boundary, and heat flux beneath the Antarctic Plate inferred from seismic velocities. *Journal of Geophysical Research: Solid Earth*, *120*(12), 8720–8742. https://doi.org/10.1002/2015JB011917

Anandakrishnan, S., Blankenship, D. D., Alley, R. B., & Stoffa, P. L. (1998). Influence of subglacial geology on the position of a West Antarctic ice stream from seismic observations. *Nature*, *394*(6688), 62–65. https://doi.org/10.1038/27889

Artemieva, I. M., & Mooney, W. D. (2001). Thermal thickness and evolution of precambrian lithosphere: A global study. *Journal of Geophysical Research*, *106*(B8), 16387–16414. https://doi.org/10.1029/2000JB900439

Beardsmore, G. R., & Cull, J. P. (2001). *Crustal heat flow: A guide to measurement and modelling*. Cambridge University Press.

Bell, R. E., Blankenship, D. D., Finn, C. A., Morse, D. L., Scambos, T. A., Brozena, J. M., & Hodge, S. M. (1998). Influence of subglacial geology on the onset of a West Antarctic ice stream from aerogeophysical observations. *Nature*, *394*(6688), 58–62. https://doi.org/10.1038/27889

Bingham, R. G., Ferraccioli, F., King, E. C., Larter, R. D., Pritchard, H. D., Smith, A. M., & Vaughan, D. G. (2012). Inland thinning of West Antarctic Ice Sheet steered along subglacial rifts. *Nature*, *487*(7408), 468–471. https://doi.org/10.1038/nature11292

Blankenship, D. D., Bentley, C. R., Rooney, S. T., & Alley, R. B. (1986). Seismic measurements reveal a saturated porous layer beneath an active Antarctic ice stream. *Nature*, *322*(6074), 54–57. https://doi.org/10.1038/322054a0

Borthwick, L., Muto, A., Anandakrishnan, S., Tinto, K., Agnew, R., Brisbourne, A., et al. (2025a). Potential fields modeling code from: Geophysical evidence of tectonic structures beneath Thwaites Glacier [Software]. *West Antarctica: influence on glacier dynamics (Version 1)*. https://doi.org/10.5281/zenodo.15225391

Borthwick, L., Muto, A., Anandakrishnan, S., Tinto, K., Agnew, R., Brisbourne, A., et al. (2025b). Results from: Geophysical evidence of tectonic structures beneath Thwaites Glacier, West Antarctica: Influence on glacier dynamics (version 1) [Dataset]. https://doi.org/10.5281/zenodo.15236557

Borthwick, L., Muto, A., Anandakrishnan, S., Tinto, K., Agnew, R., Brisbourne, A., et al. (2025c). Seismic data from: Geophysical evidence of tectonic structures beneath Thwaites Glacier [Dataset]. *West Antarctica: influence on glacier dynamics (Version 1)*. https://doi.org/10.5281/zenodo.15108815

Borthwick, L., Muto, A., Anandakrishnan, S., Tinto, K., Agnew, R., Brisbourne, A., et al. (2025d). Seismic travel time inversion code from: Geophysical evidence of tectonic structures beneath Thwaites Glacier [Software]. *West Antarctica: influence on glacier dynamics (Version 1)*. https://doi.org/10.5281/zenodo.15230759

Brocher, T. M. (2005). Empirical relations between elastic wavespeeds and density in the earth's crust. *Bulletin of the Seismological Society of America*, *95*(6), 2081–2092. https://doi.org/10.1785/0120050077

Burton-Johnson, A., Dziadek, R., & Martin, C. (2020). Review article: Geothermal heat flow in Antarctica: Current and future directions. *The Cryosphere*, *14*(11), 3843–3873. https://doi.org/10.5194/tc-14-3843-2020

Carson, C. J., McLaren, S., Roberts, J. L., Boger, S. D., & Blankenship, D. D. (2014). Hot rocks in a cold place: High sub-glacial heat flow in East Antarctica. *Journal of the Geological Society*, *171*(1), 9–12. https://doi.org/10.1144/jgs2013-030

Christoffersen, P., Bougamont, M., Carter, S. P., Fricker, H. A., & Tulaczyk, S. (2014). Significant groundwater contribution to Antarctic ice streams hydrologic budget. *Geophysical Research Letters*, *41*(6), 2003–2010. https://doi.org/10.1002/2014GL059250

Clyne, E. R., Anandakrishnan, S., Muto, A., Alley, R. B., & Voigt, D. E. (2020). Interpretation of topography and bed properties beneath Thwaites Glacier, West Antarctica using seismic reflection methods. *Earth and Planetary Science Letters*, *550*, 116543. https://doi.org/10.1016/j.epsl.2020.116543

Cochran, J. R., Elieff, S., Tinto, J., & Charles, K. (2011). IceBridge gravity instrument performance and data assessment (tech. Rep.).

Cuffey, K. M., & Paterson, W. S. B. (2010). *The physics of glaciers* (4th ed.). Butterworth-Heinemann.

Damiani, T. M., Jordan, T., Ferraccioli, F., Young, D. A., & Blankenship, D. D. (2014). Variable crustal thickness beneath Thwaites Glacier revealed from airborne gravimetry, possible implications for geothermal heat flux in West Antarctica. *Earth and Planetary Science Letters*, *407*, 109–122. https://doi.org/10.1016/j.epsl.2014.09.023

DeConto, R. M., Pollard, D., Alley, R. B., Velicogna, I., Gasson, E., Gomez, N., et al. (2021). The Paris Climate Agreement and future sea-level rise from Antarctica. *Nature*, *593*(7857), 83–89. https://doi.org/10.1038/s41586-021-03427-0

Diehl, T. M., Holt, J. W., Blankenship, D. D., Young, D. A., Jordan, T., & Ferraccioli, F. (2008). First airborne gravity results over the thwaites glacier catchment, West Antarctica. *Geochemistry, Geophysics, Geosystems*, *9*(4), Q04011. https://doi.org/10.1029/2007GC001878

Dunham, C. K., O'Donnell, J. P., Stuart, G. W., Brisbourne, A. M., Rost, S., Jordan, T., et al. (2020). A joint inversion of receiver function and Rayleigh wave phase velocity dispersion data to estimate crustal structure in West Antarctica. *Geophysical Journal International*, *223*(3), 1644–1657. https://doi.org/10.1093/gji/ggaa398

Dziadek, R., Ferraccioli, F., & Gohl, K. (2021). High geothermal heat flow beneath Thwaites Glacier in West Antarctica inferred from aeromagnetic data. *Communications Earth & Environment*, *2*(1), 1–6. https://doi.org/10.1038/s43247-021-00242-3

Engelhardt, H., & Kamb, B. (1998). Basal sliding of ice stream B, West Antarctica. *Journal of Glaciology*, *44*(147), 223–230. https://doi.org/10.3189/S0022143000002562

Ferraccioli, F., Armadillo, E., Zunino, A., Bozzo, E., Rocchi, S., & Armienti, P. (2009). Magmatic and tectonic patterns over the Northern Victoria land sector of the transantarctic mountains from new aeromagnetic imaging. *Tectonophysics*, *478*(1–2), 43–61. https://doi.org/10.1016/j.tecto.2008.11.028

Ferraccioli, F., Bozzo, E., & Damaske, D. (2002). Aeromagnetic signatures over western marie byrd land provide insight into magmatic arc basement, mafic magmatism and structure of the eastern ross sea rift flank. *Tectonophysics*, *347*(1), 139–165. https://doi.org/10.1016/s0040-1951(01)00242-6

Fricker, H. A., Scambos, T., Bindschadler, R., & Padman, L. (2007). An active subglacial water system in West Antarctica mapped from space. *Science*, *315*(5818), 1544–1548. https://doi.org/10.1126/science.1136897

Ghirotto, A., Zunino, A., Armadillo, E., & Mosegaard, K. (2021). Magnetic anomalies caused by 2D polygonal structures with uniform arbitrary polarization: New insights from analytical/numerical comparison among available algorithm formulations. *Geophysical Research Letters*, *48*(7), 1–13. https://doi.org/10.1029/2020GL091732

Gooch, B. T., Young, D. A., & Blankenship, D. D. (2016). Potential groundwater and heterogeneous heat source contributions to ice sheet dynamics in critical submarine basins of East Antarctica. *Geochemistry, Geophysics, Geosystems*, *17*(2), 395–409. https://doi.org/10.1002/2015GC006117

Greene, C. A., Gwyther, D. E., & Blankenship, D. D. (2017). Antarctic mapping tools for matlab. *Computers & Geosciences*, *104*, 151–157. https://doi.org/10.1016/j.cageo.2016.08.003

Holschuh, N., Christianson, K., Paden, J., Alley, R. B., & Anandakrishnan, S. (2020). Linking postglacial landscapes to glacier dynamics using swath radar at Thwaites glacier, Antarctica. *Geology*, *48*(3), 268–272. https://doi.org/10.1130/G46772.1

Horgan, H. J., Anandakrishnan, S., Alley, R. B., Burkett, P. G., & Peters, L. E. (2011). Englacial seismic reflectivity: Imaging crystal-orientation fabric in West Antarctica. *Journal of Glaciology*, *57*(204), 639–650. https://doi.org/10.3189/002214311797409686

Howat, I., Porter, C., Noh, M.-J., Husby, E., Khuvis, S., Danish, E., et al. (2022). The reference elevation model of Antarctica - Mosaics, Version 2. *Harvard Dataverse*. https://doi.org/10.7910/DVN/EBW8UC

Jordan, T., Ferraccioli, F., Vaughan, D. G., Holt, J. W., Corr, H., Blankenship, D. D., & Diehl, T. M. (2010). Aerogravity evidence for major crustal thinning under the Pine Island Glacier region (West Antarctica). *Geological Society of America Bulletin*, *122*(5–6), 714–726. https://doi.org/10.1130/B26417.1

Jordan, T., Riley, T. R., & Siddoway, C. S. (2020). The geological history and evolution of West Antarctica. *Nature Reviews Earth & Environment*, *1*(2), 117–133. https://doi.org/10.1038/s43017-019-0013-6

Jordan, T., & Robinson, C. (2021a). Processed line aerogravity data over the Thwaites Glacier region (2019/20 season) (Version 1.0) [Dataset]. *NERC EDS UK Polar Data Centre*. https://doi.org/10.5285/af14076f-f0c4-479f-b38f-6aa0b7c7d314

Jordan, T., & Robinson, C. (2021b). Processed line aeromagnetic data over the Thwaites glacier region (2019/2020 season) (Version 1.0) [Dataset]. *NERC EDS UK Polar Data Centre*. https://doi.org/10.5285/EB6BF8DF-EA87-4C3C-8F27-33FA8D5AC663

Jordan, T., Thompson, S., Kulessa, B., & Ferraccioli, F. (2023). Geological sketch map and implications for ice flow of Thwaites Glacier, West Antarctica, from integrated aerogeophysical observations. *Science Advances*, *9*(22), eadf2639. https://doi.org/10.1126/sciadv.adf2639

Joughin, I., Tulaczyk, S., Bamber, J. L., Blankenship, D., Holt, J. W., Scambos, T., & Vaughan, D. G. (2009). Basal conditions for Pine Island and Thwaites Glaciers, West Antarctica, determined using satellite and airborne data. *Journal of Glaciology*, *55*(190), 245–257. https://doi.org/10.3189/002214309788608705

Kalberg, T., & Gohl, K. (2014). The crustal structure and tectonic development of the continental margin of the Amundsen sea embayment, West Antarctica: Implications from geophysical data. *Geophysical Journal International*, *198*(1), 327–341. https://doi.org/10.1093/gji/ggu118

Kalberg, T., Gohl, K., Eagles, G., & Spiegel, C. (2015). Rift processes and crustal structure of the Amundsen Sea Embayment, West Antarctica, from 3D potential field modelling. *Marine Geophysical Researches*, *36*(4), 263–279. https://doi.org/10.1007/s11001-015-9261-0

Kamb, B. (2001). Basal zone of the West Antarctic Ice streams and its role in lubrication of their rapid motion. *Antarctic Research Series*, *77*, 157–199. https://doi.org/10.1029/ar077p0157

Karner, G. D., Studinger, M., & Bell, R. E. (2005). Gravity anomalies of sedimentary basins and their mechanical implications: Application to the Ross Sea basins, West Antarctica. *Earth and Planetary Science Letters*, *235*(3–4), 577–596. https://doi.org/10.1016/j.epsl.2005.04.016

Keller, G. R., Prodehl, C., Mechie, J., Fuchs, K., Khan, M. A., Maguire, P. K., et al. (1994). The East African rift system in the light of KRISP 90. *Tectonophysics*, *236*(1–4), 465–483. https://doi.org/10.1016/0040-1951(94)90190-2

Killingbeck, S., Kulessa, B., Brisbourne, A., Pearce, R., Borthwick, L., Napoleoni, F., et al. (2024). Magnetotelluric imaging of subglacial conditions and crustal structure beneath Thwaites Glacier and WAIS Divide. In *Abstract C53C-02. Paper presented at the AGU fall meeting 2024 Abstracts*.

Koellner, S., Parizek, B. R., Alley, R. B., Muto, A., & Holschuh, N. (2019). The impact of spatially-variable basal properties on outlet glacier flow. *Earth and Planetary Science Letters*, *515*, 200–208. https://doi.org/10.1016/j.epsl.2019.03.026

Larour, E., Seroussi, H., Adhikari, S., Ivins, E., Caron, L., Morlighem, M., & Schlegel, N. (2019). Slowdown in Antarctic mass loss from solid Earth and sea-level feedbacks. *Science*, *364*(6444), eaav7908. https://doi.org/10.1126/science.aav7908

LeMasurier, W. E. (2008). Neogene extension and basin deepening in the West Antarctic rift inferred from comparisons with the East African rift and other analogs. *Geology*, *36*(3), 247–250. https://doi.org/10.1130/G24363A.1

Mavko, G. M., Mukerji, T., & Dvorkin, J. (2020). *The rock physics handbook*. Cambridge University Press.

McCormack, F. S., Warner, R. C., Seroussi, H., Dow, C. F., Roberts, J. L., & Treverrow, A. (2022). Modeling the deformation regime of Thwaites Glacier, west Antarctica, using a simple flow relation for ice anisotropy (estar). *Journal of Geophysical Research: Earth Surface*, *127*(3), e2021JF006332. https://doi.org/10.1029/2021JF006332

Morlighem, M. (2022). MEaSUREs BedMachine Antarctica, Version 3. *NASA National Snow and Ice Data Center Distributed Active Archive Center*. https://doi.org/10.5067/FPSU0V1MWUB6

Morlighem, M., Goldberg, D., Barnes, J. M., Bassis, J. N., Benn, D. I., Crawford, A. J., et al. (2024). The West Antarctic Ice Sheet may not be vulnerable to marine ice cliff instability during the 21st century. *Science Advances*, *10*(34), eado7794. https://doi.org/10.1126/sciadv.ado7794

Morlighem, M., Rignot, E., Binder, T., Blankenship, D., Drews, R., Eagles, G., et al. (2020). Deep glacial troughs and stabilizing ridges unveiled beneath the margins of the Antarctic ice sheet. *Nature Geoscience*, *13*(2), 132–137. https://doi.org/10.1038/s41561-019-0510-8

Mouginot, J., Rignot, E., Bjørk, A. A., van den Broeke, M., Millan, R., Morlighem, M., et al. (2019). Forty-six years of Greenland Ice Sheet mass balance from 1972 to 2018. *Proceedings of the National Academy of Sciences of the United States of America*, *116*(19), 9239–9244. https://doi.org/10.1073/pnas.1904242116

Mouginot, J., Rignot, E., & Scheuchl, B. (2014). Sustained increase in ice discharge from the Amundsen Sea Embayment, West Antarctica, from 1973 to 2013. *Geophysical Research Letters*, *41*(5), 1576–1584. https://doi.org/10.1002/2013GL059069

Muto, A., Anandakrishnan, S., Alley, R. B., Horgan, H. J., Parizek, B. R., Koellner, S., et al. (2019). Relating bed character and subglacial morphology using seismic data from thwaites glacier, west Antarctica. *Earth and Planetary Science Letters*, *507*, 199–206. https://doi.org/10.1016/j.epsl.2018.12.008

Naughten, K. A., Holland, P. R., & De Rydt, J. (2023). Unavoidable future increase in West Antarctic ice-shelf melting over the twenty-first century. *Nature Climate Change*, *13*(11), 1222–1228. https://doi.org/10.1038/s41558-023-01818-x

Parizek, B. R., Christianson, K., Anandakrishnan, S., Alley, R. B., Walker, R. T., Edwards, R. A., et al. (2013). Dynamic (in)stability of Thwaites Glacier, West Antarctica. *Journal of Geophysical Research: Earth Surface*, *118*(2), 638–655. https://doi.org/10.1002/jgrf.20044

Paxman, G. J., Austermann, J., & Hollyday, A. (2022). Total isostatic response to the complete unloading of the Greenland and Antarctic Ice Sheets. *Scientific Reports*, *12*(1), 1–11. https://doi.org/10.1038/s41598-022-15440-y

Peters, L. E., Anandakrishnan, S., Alley, R. B., Winberry, J. P., Voigt, D. E., Smith, A. M., & Morse, D. L. (2006). Subglacial sediments as a control on the onset and location of two Siple Coast ice streams, West Antarctica. *Journal of Geophysical Research*, *111*(1), 1–14. https://doi.org/10.1029/2005JB003766

Pollack, H. N., & Chapman, D. S. (1977). Mantle heat flow. *Earth and Planetary Science Letters*, *34*(2), 174–184. https://doi.org/10.1016/0012-821x(77)90002-4

Pollard, D., DeConto, R. M., & Alley, R. B. (2015). Potential Antarctic Ice Sheet retreat driven by hydrofracturing and ice cliff failure. *Earth and Planetary Science Letters*, *412*, 112–121. https://doi.org/10.1016/j.epsl.2014.12.035

Prodehl, C., Jacob, A. W., Thybo, H., Dindi, E., & Stangl, R. (1994). Crustal structure on the northeastern flank of the Kenya rift. *Tectonophysics*, *236*(1–4), 271–290. https://doi.org/10.1016/0040-1951(94)90180-5

Ramirez, C., Nyblade, A., Hansen, S. E., Wiens, D. A., Anandakrishnan, S., Aster, R. C., et al. (2016). Crustal and upper-mantle structure beneath ice-covered regions in Antarctica from S-wave receiver functions and implications for heat flow. *Geophysical Journal International*, *204*(3), 1636–1648. https://doi.org/10.1093/gji/ggv542

Ringler, A. T., Anthony, R. E., Karplus, M. S., Holland, A. A., & Wilson, D. C. (2018). Laboratory tests of three Z-land Fairfield nodal 5-Hz, three-component Sensors. *Seismological Research Letters*, *89*(5), 1601–1608. https://doi.org/10.1785/0220170236

Rocchi, S., LeMasurier, W. E., & Di Vincenzo, G. (2006). Oligocene to holocene erosion and glacial history in marie byrd land, west Antarctica, inferred from exhumation of the dorrel rock intrusive complex and from volcano morphologies. *GSA Bulletin*, *118*(7–8), 991–1005. https://doi.org/10.1130/B25675.1

Rooney, S., Blankenship, D., Alley, R., & Bentley, C. (1991). Seismic reflection profiling of a sediment-filled graben beneath ice stream B, West Antarctica. In M. Thomson, J. Crame, & J. Thomson (Eds.), *Geological evolution of Antarctica* (pp. 261–265). Cambridge University Press.

Roy, L., Sen, M. K., McIntosh, K., Stoffa, P. L., & Nakamura, Y. (2005). Joint inversion of first arrival seismic travel-time and gravity data. *Journal of Geophysics and Engineering*, *2*(3), 277–289. https://doi.org/10.1088/1742-2132/2/3/011

Rücker, C., Günther, T., & Wagner, F. M. (2017). pyGIMLi: An open-source library for modelling and inversion in geophysics. *Computers & Geosciences*, *109*, 106–123. https://doi.org/10.1016/j.cageo.2017.07.011

Sandrin, A., & Thybo, H. (2008). Seismic constraints on a large mafic intrusion with implications for the subsidence history of the Danish Basin. *Journal of Geophysical Research*, *113*(9), B09402. https://doi.org/10.1029/2007JB005067

Scambos, T. A., Bell, R. E., Alley, R. B., Anandakrishnan, S., Bromwich, D. H., Brunt, K., et al. (2017). *How much, how fast? A science review and outlook for research on the instability of Antarctica's Thwaites Glacier in the 21st century*. Elsevier B.V. (Vol. 153, pp. 16–34). https://doi.org/10.1016/j.gloplacha.2017.04.008

Schoof, C. (2012). Marine ice sheet stability. *Journal of Fluid Mechanics*, *698*, 62–72. https://doi.org/10.1017/jfm.2012.43

Schroeder, D. M., Blankenship, D. D., Young, D. A., Witus, A. E., & Anderson, J. B. (2014). Airborne radar sounding evidence for deformable sediments and outcropping bedrock beneath Thwaites Glacier, West Antarctica. *Geophysical Research Letters*, *41*(20), 7200–7208. https://doi.org/10.1002/2014GL061645

Schwans, E., Parizek, B. R., Alley, R. B., Anandakrishnan, S., & Morlighem, M. M. (2023). Model insights into bed control on retreat of Thwaites Glacier, West Antarctica. *Journal of Glaciology*, *69*(277), 1241–1259. https://doi.org/10.1017/jog.2023.13

Shepherd, T., Bamber, J., & Ferraccioli, F. (2006). Subglacial geology in Coats Land, East Antarctica, revealed by airborne magnetics and radar sounding. *Earth and Planetary Science Letters*, *244*(1–2), 323–335. https://doi.org/10.1016/j.epsl.2006.01.068

Siddoway, C. (2008). Tectonics of the West Antarctic Rift System: New light on the history and dynamics of distributed intracontinental extension. In A. K. Cooper, P. J. Barrett, H. Stagg, B. Storey, E. Stump, W. Wise, & the 10th ISAES Editorial Team (Eds.), *Antarctica: A keystone in a changing World. Proceedings of the 10th international symposium on Antarctic Earth sciences* (pp. 91–114). The National Academies Press.

Siegert, M. J., Kulessa, B., Bougamont, M., Christoffersen, P., Key, K., Andersen, K. R., et al. (2018). *Antarctic subglacial groundwater: A concept paper on its measurement and potential influence on ice flow*. Geological Society, London, Special Publications. (Vol. 461, pp. 197–213). https://doi.org/10.1144/SP461.8

Sippel, J., Meeßen, C., Cacace, M., Mechie, J., Fishwick, S., Heine, C., et al. (2017). The Kenya rift revisited: Insights into lithospheric strength through data-driven 3-D gravity and thermal modelling. *Solid Earth*, *8*(1), 45–81. https://doi.org/10.5194/se-8-45-2017

Slagstad, T. (2008). Radiogenic heat production of Archaean to Permian geological provinces in Norway. *Norwegian Journal of Geology*, *88*(3), 149–166.

Smith, A. M., Jordan, T., Ferraccioli, F., & Bingham, R. G. (2013). Influence of subglacial conditions on ice stream dynamics: Seismic and potential field data from Pine Island Glacier, West Antarctica. *Journal of Geophysical Research: Solid Earth*, *118*(4), 1471–1482. https://doi.org/10.1029/2012JB009582

Swain, C. J., & Kirby, J. F. (2021). Effective elastic thickness map reveals subglacial structure of east Antarctica. *Geophysical Research Letters*, *48*(4), 1–11. https://doi.org/10.1029/2020GL091576

Swain, C. J., Maguire, P. K., & Khan, M. A. (1994). Geophysical experiments and models of the Kenya Rift before 1989. *Tectonophysics*, *236*(1–4), 23–32. https://doi.org/10.1016/0040-1951(94)90167-8

The IMBIE Team. (2018). Mass balance of the antarctic ice sheet from 1992 to 2017. *Nature*, *558*(7709), 219–222. https://doi.org/10.1038/s41586-018-0179-y

Tinto, K. J., & Bell, R. E. (2011). Progressive unpinning of Thwaites Glacier from newly identified offshore ridge: Constraints from aerogravity. *Geophysical Research Letters*, *38*(20). https://doi.org/10.1029/2011GL049026

Uieda, L., Oliveira, V., & Barbosa, V. (2013). Modeling the Earth with Fatiando a Terra. In *Proceedings of the python in science conference*. https://doi.org/10.25080/majora-8b375195-010

Vitorello, I., & Pollack, H. N. (1980). On the variation of continental heat flow with age and the thermal evolution of continents. *Journal of Geophysical Research*, *85*(B2), 983–995. https://doi.org/10.1029/jb085ib02p00983

Watts, A. (1988). Gravity anomalies, crustal structure and flexure of the lithosphere at the Baltimore Canyon Trough. *Earth and Planetary Science Letters*, *89*(2), 221–238. https://doi.org/10.1016/0012-821X(88)90174-4

Watts, A. (2023). *Isostasy and flexure of the lithosphere* (2nd ed.). Cambridge University Press.

Watts, A., & Burov, E. (2003). Lithospheric strength and its relationship to the elastic and seismogenic layer thickness. *Earth and Planetary Science Letters*, *213*(1–2), 113–131. https://doi.org/10.1016/S0012-821X(03)00289-9

Weertman, J. (1974). Stability of the junction of an ice sheet and an ice shelf. *Journal of Glaciology*, *13*(67), 3–11. https://doi.org/10.3189/S0022143000023327

Winberry, J. P., & Anandakrishnan, S. (2004). Crustal structure of the West Antarctic rift system and marie byrd land hotspot. *Geology*, *32*(11), 977–980. https://doi.org/10.1130/G20768.1

Won, I. J., & Bevis, M. (1987). Computing the gravitational and magnetic anomalies due to a polygon: Algorithms and Fortran subroutines. *Geophysics*, *52*(2), 232–238. https://doi.org/10.1190/1.1442298

Zelt, C. A., & Smith, R. B. (1992). Seismic traveltime inversion for 2-d crustal velocity structure. *Geophysical Journal International*, *108*(1), 16–34. https://doi.org/10.1111/j.1365-246x.1992.tb00836.x

Zhou, Z., Wiens, D. A., Shen, W., Aster, R. C., Nyblade, A., & Wilson, T. J. (2022). Radial anisotropy and sediment thickness of west and Central Antarctica estimated from Rayleigh and Love wave velocities. *Journal of Geophysical Research: Solid Earth*, *127*(3), 1–23. https://doi.org/10.1029/2021JB022857

Zoet, L. K., & Iverson, N. R. (2020). A slip law for glaciers on deformable beds. *Science*, *368*(6486), 76–78. https://doi.org/10.1126/science.aaz1183